Spike-frequency dependent inhibition and potentiation of neural activity by ultrasound

Martin Loynaz Prieto[1*], Kamyar Firouzi[2], Butrus T. Khuri-Yakub[2], Daniel V. Madison[1], and Merritt Maduke[1*]

[1]Department of Molecular and Cellular Physiology, Stanford University
[2]E. L. Ginzton Laboratory, Stanford University

*Corresponding authors

Condensed title: Spike-Rate-Dependent Neuromodulation by Ultrasound

SUMMARY Prieto et al. describe how ultrasound can either inhibit or potentiate action potential firing in hippocampal pyramidal neurons and demonstrate that these effects can be explained by increased potassium conductance.

ABSTRACT

Ultrasound can modulate action potential firing *in vivo* and *in vitro*, but the mechanistic basis of this phenomenon is not well understood. To address this problem, we used patch-clamp recording to quantify the effects of focused, high-frequency (43 MHz) ultrasound on evoked action potential firing in CA1 pyramidal neurons in acute rodent hippocampal brain slices. We find that ultrasound can either inhibit or potentiate firing in a spike-frequency-dependent manner: at low (near-threshold) input currents and low firing frequencies, ultrasound inhibits firing, while at higher input currents and higher firing frequencies, ultrasound potentiates firing. The net result of these two competing effects is that ultrasound increases the threshold current for action potential firing, the slope of frequency-input curves, and the maximum firing frequency. In addition, ultrasound slightly hyperpolarizes the resting membrane potential, decreases action potential width, and increases the depth of the afterhyperpolarization. All of these results can be explained by the hypothesis that ultrasound activates a sustained potassium conductance. According to this hypothesis, increased outward potassium currents hyperpolarize the resting membrane potential and inhibit firing at near-threshold input currents, but potentiate firing in response to higher input currents by limiting inactivation of voltage-dependent sodium channels during the action potential. This latter effect is a consequence of faster action-potential repolarization, which limits inactivation of voltage-dependent sodium channels, and deeper (more negative) afterhyperpolarization, which increases the rate of recovery from inactivation. Based on these results we propose that ultrasound activates thermosensitive and mechanosensitive, voltage-insensitive two-pore-domain potassium (K2P) channels, through heating or mechanical effects of acoustic radiation force. Finite-element modelling of the effects of ultrasound on brain tissue suggests that the effects of ultrasound on firing frequency are caused by a small (less than 2°C) increase in temperature, with possible additional contributions from mechanical effects.

INTRODUCTION

Ultrasound can non-invasively modulate action potential activity in neurons *in vivo* and *in vitro*, with improved depth penetration and spatial resolution relative to other non-invasive neuromodulation modalities, and it may therefore become an important new technology in basic and clinical neuroscience (Fry et al., 1958; Gavrilov et al., 1996; Tufail et al., 2010; Bystritsky et al., 2011; Fomenko et al., 2018; Blackmore et al., 2019). Investigation of this phenomenon has predominantly focused on low-frequency ultrasound (defined here as less than 3 MHz, although there is no firmly defined boundary between “high” and “low” frequency in the neuromodulation field), but higher ultrasound frequencies have also been shown to modulate action potential firing *in vitro* (Menz et al., 2013; Menz et al., 2019) and to directly modulate ion channel activity in heterologous systems (Kubanek et al., 2016; Prieto et al., 2018). The focus on lower frequency ultrasound is understandable, since envisioned clinical applications involving transcranial focused ultrasound have been a primary motivation for research on ultrasound neuromodulation, and loss of ultrasound power due to attenuation in the skull limits these applications to low frequency ultrasound. For applications in which transmission through the skull does not impose limits on frequency, such as *in vitro* studies, neuromodulation in the peripheral nervous system (Downs et al., 2018; Cotero et al., 2019; Zachs et al., 2019), neuromodulation using subcranial implants, or neuromodulation in experimental animal model systems involving craniotomies or acoustically transparent cranial windows, high frequencies have a distinct advantage in terms of the greater spatial resolution that can be achieved.

These applications motivate investigation of the fundamental physical, cellular, and molecular mechanisms underlying neuromodulation by high-frequency ultrasound, which are all not well understood. It remains an open question to what extent these mechanisms overlap for high- and low-frequency ultrasound neuromodulation. In terms of the basic physical mechanism by which acoustic energy is transduced into effects on biological tissue, most proposed mechanisms for ultrasound neuromodulation involve either heating due to absorption of acoustic

energy (Hand, 1998), mechanical effects of acoustic radiation force (Duck, 1998; Sarvazyan et al., 2010), or effects of cavitation (the nucleation, growth, oscillation, and sometimes collapse, of microscopic gas bubbles) (Leighton, 1998; Wu and Nyborg, 2008; Krasovitski et al., 2011; Plaksin et al., 2016). Of these, the first two increase with acoustic frequency, while the probability of cavitation decreases with acoustic frequency. There are also many unanswered questions at the cellular level. Both excitatory and inhibitory effects of ultrasound have been observed using direct or indirect measures of neural activity at the population level (Bystritsky et al., 2011; Blackmore et al., 2019), but it is unclear whether the direct effect of ultrasound at the cellular level is excitatory or inhibitory. Of course, the answer to this question could depend on any number of possible relevant biological and experimental variables, such as species, tissue, specific neural subtype, ultrasound stimulus parameters, or whether effects on intrinsic or evoked activity are measured. For example, a cellular-level excitatory effect, specific to GABAergic interneurons, could produce an inhibitory effect at the population level. This leads to the question of whether certain subpopulations of neurons are more sensitive to ultrasound than others, and if so, what are the specific molecular mechanisms underlying the differences in sensitivity. Do certain ion channels respond directly to ultrasound? What biophysical properties might account for the sensitivity of these channels to ultrasound, and how might cell-type specific differences in the density and localization of these channels, and the way in which they interact with other ion channels to regulate action potential firing, produce differences in the response to ultrasound?

One reason there are so many outstanding questions regarding ultrasound neuromodulation is that patch-clamp recordings of the effects of ultrasound on action potential firing in neurons have been unavailable. At low ultrasound frequencies, we (Prieto et al., 2018) and others (Tyler et al., 2008) have found that patch-clamp seals are extremely unstable in the presence of ultrasound at low frequencies, precluding detailed, mechanistic studies of ultrasound neuromodulation with this technique, which provides quantitative information on action potential timing and dynamics unobtainable with other techniques. However, we have previously shown

52 that stable patch-clamp recordings can be achieved using ultrasound at the frequency of 43 MHz
53 (Prieto et al., 2018). Here, we use patch-clamp recording to measure the effects of ultrasound at
54 43 MHz and 50 W/cm^2 on action-potential firing in response to injected current in pyramidal
55 neurons of the CA1 layer of the hippocampus in acute rodent brain slices. We find that ultrasound
56 has a bidirectional, spike-frequency dependent effect on excitability, and that this and other
57 observed neurophysiological effects of ultrasound can be explained by activation by ultrasound
58 of a steady K^+ current, resembling that of two pore domain potassium channels (K2P channels).
59

60 **MATERIALS AND METHODS**

61 *Slice preparation.* Brain slices were prepared from male Sprague-Dawley rats, 35-50 days old.
62 Rats were anesthetized with isofluorane and decapitated, and the brain was immediately removed
63 and placed in ice-cold artificial cerebral spinal fluid (ACSF), bubbled with 95% O_2 and 5% CO_2.
64 The hippocampus was dissected out and placed on the slicing apparatus, consisting of a manual
65 micrometer and a gravity-driven vertical slicing mechanism, with the CA1 layer oriented
66 approximately parallel to the slicing blade. Slices (500 microns thick) were prepared and then
67 stored in a humidified chamber with an atmosphere of 95% O_2/5% CO_2, resting on a square of
68 filter paper placed on a dish of ACSF. Slices were used within 1-6 hours of slice preparation.
69 Animals were handled in accordance with protocols approved by Stanford University's Institutional
70 Animal Care and Use Committee.
71

72 *Ultrasound.* Continuous wave ultrasound at 43 MHz and 50 W/cm^2 was applied to brain slices
73 using a set-up similar to that we previously used for our experiments on cultured cells (Prieto et
74 al., 2018), except that the tissue was visualized with a dissecting microscope at low magnification.
75 The bottom of the experimental chamber was a 25-micron film of polystyrene, plasma-treated with
76 a Harrick plasma cleaner (Harrick Plasma, Ithaca, NY). Ultrasound was transmitted from below
77 (through the polystyrene film) with the sound beam perpendicular to the bottom of the chamber.

78 The 43 MHz transducer was a custom-built device, calibrated as described previously (Prieto et
79 al., 2013), excited using an ENI 403LA (37 dB) amplifier (ENI, Rochester, NY). The focal volume
80 of the transducer is approximately a cylinder 90 microns in diameter by 500 microns long, and the
81 focal distance is approximately 4.2 mm. The set-up was based on the stage from a Zeiss
82 Axioskop-2 microscope (Zeiss Microscopes, Jena, Germany), with the housing for the sub-stage
83 condenser modified to accommodate the transducer, such that the position of the transducer
84 could be adjusted using the controls for alignment of the condenser, and the position of the tissue
85 sample relative to the transducer could be adjusted with the microscope stage. The transducer
86 was coupled to the polystyrene film at the bottom of the experimental chamber using a small
87 volume of distilled water held in place by a rubber O-ring attached to the tip of the transducer with
88 silicone grease. The focal volume of the transducer was aligned along the z-axis using a pulse-
89 echo protocol, adjusting the height of the transducer to maximize the echo signal from the bottom
90 of the empty chamber. The focus was aligned in the x-y plane by adding to the chamber a small
91 volume of ACSF, barely sufficient to cover the bottom of the chamber, such that a thin layer of
92 solution was spread over the bottom of the chamber. Ultrasound pulses, one second in length,
93 were then applied, raising a mound of fluid at the focus of the transducer (due to the radiation
94 force produced by reflection of the acoustic wave at the interface between the solution and the air
95 above it (Duck, 1998)). The mound of fluid was then aligned in the x-y plane to the center of a
96 reticle in one eyepiece of the dissecting microscope, and, after adding additional ACSF and the
97 tissue sample to the chamber, the center of the reticle was aligned with the region of the tissue
98 targeted for patch-clamp recording. The ultrasound intensity (50 W/cm^2) is the spatial peak, pulse
99 average intensity for the free field. The interval between ultrasound applications was at least 12
100 seconds.
101
102 *Electrophysiology.* Current clamp recordings were performed using an Axon Instruments
103 Axoclamp-2B amplifier operating in “Bridge” mode and Digidata 1330A digitizer with pClamp

104 software (Molecular Devices, Sunnyvale, CA), except for the preliminary experiments in
105 Supplemental Figure 1, which were performed with an Axon Instruments Axopatch 200B amplifier
106 (Molecular Devices, Sunnyvale, CA). Patch-clamp recording was performed using a “blind-patch”
107 approach (Blanton et al., 1989; Malinow and Tsien, 1990; Castaneda-Castellanos et al., 2006), in
108 which the recording pipette was positioned above the CA1 layer of the hippocampus, as identified
109 visually at low magnification, and then slowly lowered into the tissue while applying positive
110 pressure to the pipette and monitoring the pipette tip resistance in voltage-clamp mode. In the
111 blind-patch approach, a small decrease in tip resistance is used to indicate possible contact of
112 the pipette tip with a neuron in the absence of the usual visual cues. Typically, the first two
113 instances of possible cell contact were not used, to avoid patching on cells at the surface of the
114 tissue that may have been damaged during the slicing procedure. Gigaseals and the subsequent
115 whole-cell recording configuration were obtained following the standard procedure in voltage-
116 clamp mode before switching to current-clamp mode. In most experiments, slices were held in
117 place with a Warner Instruments RC-22 slice anchor (Harvard Bioscience, Hamden, CT); the
118 experiments in Supplemental Figure 1 and some of the experiments in Figure 1E were performed
119 without a slice anchor. No obvious effects of the slice anchor on the ultrasound response were
120 noted. Series resistance, monitored and compensated throughout the recording, was between 30
121 and 100 M• . All of the neurons used for experiments could be unambiguously identified as
122 pyramidal cells by their distinct adaptive firing patterns in response to 2-s current steps. Current
123 records were low-pass filtered at 10 kHz and sampled at 100 kHz. Brain slices were continuously
124 perfused with ACSF (in mM: 119 NaCl, 2.5 KCl, 1.3 $MgSO_4$, 2.5 $CaCl_2$, 1 NaH_2PO_4, 26.2 $NaHCO_3$,
125 11 glucose), bubbled with 95% O_2/5% CO_2, at ~100-250 mL/hour. The internal solution was (in
126 mM): 126 K-gluconate, 4 KCl, 10 HEPES, 4 Mg-ATP, 0.3 Na_2GTP, 10 Na-phosphocreatine, 10
127 sucrose, and 50 U/mL creatine phosphokinase (porcine), pH 7.2 (KOH). This internal solution
128 contains an ATP-regenerating system (phosphocreatine and creatine phosphokinase) because
129 we found that the strength of the response to ultrasound was unstable, gradually declining over

130 the course of a recording unless the ATP-regenerating system was included (Supplemental
131 Figure 2). Na-phosphocreatine was obtained from Abcam and creatine phosphokinase was
132 obtained from EMD Millipore. All other salts and chemicals were obtained from either Sigma-
133 Aldrich or Fisher Scientific. (For some of the preliminary recordings shown in Figure 1E, the
134 creatine phosphokinase was omitted from the internal solution, or a different internal solution,
135 containing 120 K-gluconate, 40 HEPES, 5 $MgCl_2$, 0.3 Na_2GTP, 2 Na_2ATP, pH 7.2 (KOH) was
136 used. Other than the instability of the ultrasound response over time in the absence of creatine
137 phosphokinase, no obvious differences in recordings with different internal solutions were noted.)
138 Because creatine phosphokinase increases the viscosity of the solution, making it difficult to
139 obtain gigaseals, a small volume of internal solution without the enzyme was added to the tip of
140 the pipette (enough to fill approximately the first 3 mm of the tip) before back-filling the pipette
141 with the enzyme-containing solution. Pipettes were pulled from thick walled glass and had
142 resistances between 5 and 10 M• • Recordings were performed at room temperature (21-23°C).
143
144 *Data analysis.* Current records were analyzed in Igor Pro (Wavemetrics, Lake Oswego, OR) with
145 user-written procedures. Action-potential threshold was defined as the point at which the first
146 derivative of the voltage reached 4% of its peak value during the rising phase of the action
147 potential. This quantitative criterion was previously found to correspond with action-potential
148 thresholds as identified visually (Khaliq and Bean, 2010; Yamada-Hanff and Bean, 2015), and we
149 found that it also works well with our data, using phase plots to visually confirm the threshold
150 value. Action-potential height was defined as the difference between the action-potential peak
151 and the action-potential threshold voltage. Action-potential width was measured at 50% of action
152 potential height defined in this manner. Threshold current levels for action-potential firing were
153 estimated based on a series of current steps in 10-pA increments. Frequency-input plots and
154 action-potential parameters (height, width, latency, and interspike intervals) were determined from
155 the average values of at least 3 trials each for the control and ultrasound conditions. Frequency-

input trials were performed alternatingly for the control and ultrasound conditions, with the first condition tested varying randomly on a cell-by-cell basis.

Average traces for analysis of the effects of ultrasound on membrane resting potential and membrane capacitance were derived from at least 3 voltage traces.

Statistical significance was assessed using paired or unpaired two-tailed Student's t-tests, with $P < 0.05$ defined as significant. Statistical analysis was performed in Microsoft Excel.

Finite-element simulations. Finite-element were performed in COMSOL (COMSOL Inc., Palo Alto, CA, USA). The simulation domain had radially symmetric geometry and was 6 mm in the axial direction. The simulation domain contained four layers of different materials: a lower layer of water (4.2 mm thick in the axial direction), followed by a layer of polystyrene (25 microns thick), followed by a layer of brain tissue (500 microns thick), followed by an upper layer of water (1.275 mm thick). The width of the simulation domain in the axial direction was 1 mm (for simulation for acoustic pressure and heating) or 5 mm (for simulation of mechanical deformation) in the axial direction. A 940-micron diameter by 100-micron height arc on the lower axial boundary of the simulation domain represented the quartz lens of the transducer.

Simulations of acoustic pressure, heating, and static displacement in response to radiation force were performed as described previously (Prieto et al., 2018). For simulation of dynamic tissue displacement in response to radiation force, the brain slice was modeled as a incompressible, linear viscoelastic material (Calhoun et al., 2019), characterized by Young's modulus, Poisson's ratio, and shear viscosity, loaded by the fluid layer above it. The polystyrene was modeled as a linear elastic material, because we determined in a series of simulations that including viscosity of the polystyrene had no effect on the tissue displacement. A time step of 0.1 ms was used for simulation of the dynamic tissue displacement. Material properties used for water, polystyrene, and brain tissue used in the simulation and sources for these values are given

181 in Table 1. Additional details on mesh size, boundary conditions, and solver configurations are
182 available in Prieto et al. (2018).
183
184 **SUMMARY OF SUPPLEMENTAL MATERIAL**
185 Supplemental materials include three figures showing: the effect of ultrasound at different
186 intensities on action potential firing frequency (Supplemental Figure 1); stabilization of the
187 response to ultrasound by an ATP-regenerating system in the internal solution (Supplemental
188 Figure 2); and effects of ultrasound on action potential height (Supplemental Figure 3).
189
190 **RESULTS**
191 We measured the effects of ultrasound on action-potential firing in hippocampal CA1 pyramidal
192 cells using the set-up shown in Figure 1A (described in *Materials and Methods*). Throughout the
193 experiments reported here, ultrasound was applied at 43 MHz and 50 W/cm^2 as a 1-s, continuous-
194 wave pulse. In an initial exploration of the effects of intensity on the ultrasound response, we
195 determined that 50 W/cm^2 had a sufficiently robust effect on firing frequency to permit quantitative
196 investigation of this effect (Supplemental Figure 1), but we did not perform a detailed investigation
197 of the intensity dependence. We chose to use continuous-wave ultrasound (without additional
198 low-frequency modulation within the pulse) because continuous-wave ultrasound was previously
199 found to be optimal for ultrasound neuromodulation of retinal ganglion cells at 43 MHz (Menz et
200 al., 2013). With these ultrasound parameters, we found robust, reproducible inhibition of action-
201 potential firing by ultrasound using the protocol illustrated in Figure 1B. In these experiments, a
202 current-injection amplitude sufficient to induce firing at an average frequency of ~4-12 Hz during
203 the first 500 ms of the current step (corresponding to the overlap between the ultrasound stimulus
204 and current step) was used. This range of firing frequencies is physiologically relevant and
205 sufficient to detect either inhibition or potentiation of firing. With these experimental conditions,
206 we established that the response to ultrasound is highly reproducible, both on a trial-by-trial basis

207 within the same cell (Figure 1C-D), and between cells, with similar effects seen in over fifty cells
208 (Figure 1E). In addition, the response to ultrasound was stable over the course of recordings
209 lasting over 30 minutes (Figure 1F, Supplemental Figure 2); in a few cases where the patch seal
210 lasted for over 90 minutes, the ultrasound response remained stable.
211
212 *Effects of ultrasound on frequency-input curves.* To explore the effects of ultrasound on excitability
213 over a wider range of firing frequencies, we generated frequency-input (f-i) curves comparing
214 average firing frequencies as a function of input current in the presence and absence of
215 ultrasound. An example f-i curve generated with the protocol illustrated in Figure 1B is shown in
216 Figure 2A, along with example voltage traces in Figure 2B. The average spike frequency during
217 the first 500 ms of the current step was compared to the spike frequency in the same time window
218 in the absence of ultrasound. To compare the effects of ultrasound across neurons, we converted
219 the f-i curves into plots of the relative increase or decrease in firing frequency as a function of the
220 input current (Figure 2C-D). These data reveal two distinct regimes with contrasting inhibitory and
221 excitatory ultrasound effects. At relatively low input currents, near the threshold for action-
222 potential firing under this current stimulation protocol, ultrasound decreases the average firing
223 frequency; while at relatively high input currents, well above the action-potential threshold,
224 ultrasound increases the average firing frequency. Between these two regimes, there is a
225 transitional region where there is little or no effect on average firing frequency, presumably due
226 to the balance between competing inhibitory and excitatory effects. Other notable effects of
227 ultrasound on the f-i curves are an increase in the threshold current for action-potential firing, an
228 increase in the slope of the f-i relationship in the approximately linear region of the f-i curve, and
229 an increase in the maximum firing frequency in the sublinear “plateau” region of the curve (Figure
230 2A). The mean (± SEM) slope of linear region of the f-i curve increased from 0.108 ± 0.007 Hz/pA
231 in the control condition to 0.145 ± 0.012 Hz/pA in the ultrasound condition; and the mean

232 maximum firing frequency increased from 23 ± 1 Hz in the control condition to 30 ± 2 Hz/pA in the
233 ultrasound condition (N = 9).

234 Action-potential firing behavior is determined by the interaction between numerous K^+,
235 Na^+, and other ionic currents (Madison and Nicoll, 1984; Bean, 2007). Some of these currents are
236 clearly identified with specific ion channel subtypes, while the molecular identity of others is still
237 uncertain. Thus, f-i curves are a complicated function of the density, localization, conductance,
238 and kinetic properties of these channels/currents. Some currents inactivate relatively rapidly and
239 only influence firing frequency during the initial response to a current step, while others continue
240 to influence firing frequency throughout the step. To explore the molecular basis of the response
241 to ultrasound, we therefore generated a second set of f-i curves with ultrasound applied 1 s after
242 the start of a 3-s current step (Figure 3A).

243 Ultrasound also has a bidirectional, spike-frequency-dependent effect on excitability when
244 it was applied 1 second after the start of a current step (Figure 3). As with ultrasound applied
245 before the start of the current step, ultrasound applied in the middle of the current step decreased
246 firing frequency in the low-firing-frequency, near-threshold region of the f-i curve, and increased
247 spike rate in the high-firing-frequency, suprathreshold region of the curve (Figure 3B-D). However,
248 the excitatory effect was more pronounced than we observed when the ultrasound pulse started
249 500 ms before the start of the current step. Here, ultrasound potentiated firing frequency by
250 several hundred percent for high input currents (Figure 3D), as compared with a maximum
251 potentiation of 49 ± 16% at 450 pA seen with the earlier ultrasound application (Figure 2C). This
252 effect can be explained by the fact that prolonged injection of high amplitude currents causes
253 accumulation of inactivation in many voltage-gated channels, which can drive pyramidal cells into
254 a refractory state where spiking is infrequent and irregular or entirely absent. (For example, the
255 voltage trace for the control condition at +450 pA in Figure 3C shows a steep decline in action
256 potential height (due to voltage-gated Na_V channel inactivation) followed by a period of no action
257 potential activity). If neurons are in this refractory state during the ultrasound application,

258 ultrasound can “rescue” firing (as in the example voltage trace for the ultrasound condition at +450
259 pA in Figure 3C). A hint of this rescue phenomenon is also seen when the ultrasound application
260 starts before the current step, as seen in the abrupt increase in the potentiation effect at +450 pA
261 (Figure 2C).
262
263 *Effects of ultrasound on interspike intervals.* To examine the effects of ultrasound on action-
264 potential firing in more detail we compared the latency to the first spike, and the intervals between
265 subsequent spikes (interspike intervals), in the control and ultrasound conditions. Figure 4A
266 shows raster plots summarizing action potential timing for individual current steps, ranging from
267 0 pA to +450 pA in 50 pA intervals, for the control (*left*) and ultrasound (*right*) conditions. To
268 summarize these results, and to account for the variability in intrinsic excitability between cells,
269 we averaged *instantaneous* firing frequencies (latency and interspike intervals) across cells firing
270 at approximately the same *average* firing frequency (either 5, 10, or 20 Hz) in the control condition
271 at whatever input current was necessary to achieve these average firing frequencies, and at the
272 same input current in the ultrasound condition (Figure 4B-E). We note, however, that this
273 averaging procedure can obscure some of the details of ultrasound’s effects. At 5 Hz the effect of
274 ultrasound applied 500 ms before the start of the current step is predominantly inhibitory (as seen
275 in the longer average latency and interspike intervals in the ultrasound as compared with the
276 control condition (Figure 4B), but the interval between the first and second spikes was actually
277 shorter in the ultrasound condition than the control condition in some cells (6 out of 13 cells in this
278 data set). This effect occurs because, even at relatively low average firing frequencies, pyramidal
279 cells will occasionally fire “doublets” or high-frequency bursts of two action potentials, in which a
280 second action potential is triggered by the after-depolarization of the initial action potential. When
281 this occurs, ultrasound decreases the interval between spikes (Figure 4E). This result indicates
282 that the mechanism by which ultrasound potentiates firing at high average firing frequencies is
283 also active under conditions of low overall average firing frequency, during localized periods of

284 high-frequency firing. A similar combination of inhibitory and excitatory effects can be observed
285 at 10 Hz and even 20 Hz (Figure 4C-D). At 20 Hz, ultrasound still increased the latency to the first
286 spike (16 ± 2 ms versus 12 ± 1 ms in the control condition; N = 12, P = 5.2 x 10^{-4}, paired, two-
287 tailed Student's t-test), despite decreasing the interspike interval for all subsequent spikes (Figure
288 4D). The effect of ultrasound was also mixed when ultrasound was applied 1 s after the start of
289 the current step (Figure 4F).
290
291 *Effects of ultrasound on resting membrane potential.* Ultrasound also has effects on resting
292 membrane potential, which can be observed by averaging several voltage traces aligned to the
293 onset of the ultrasound pulse, in the absence of injected current. As shown in Figure 5A,
294 ultrasound has a slight hyperpolarizing effect on resting membrane potential. The average voltage
295 traces also show another interesting effect of ultrasound. In addition to the relatively constant
296 hyperpolarization, there is a transient *depolarization* of the resting membrane potential, preceding
297 the hyperpolarization effect and acting on a faster time scale, at the onset of the ultrasound pulse;
298 this transient depolarization is matched by a roughly symmetrical transient hyperpolarization at
299 the offset of the pulse (Figure 5A, *arrows*). The symmetrical, on/off nature of these transients
300 suggests that they are caused by changes in membrane capacitance, as does the fact that they
301 occur much faster than the steady-state changes in resting membrane potential (Figure 5A-C).
302 (Changes in membrane potential due to changes in capacitance can occur much faster than those
303 due to ionic currents because they do not involve actual redistribution of charges across the
304 membrane and are therefore not limited by membrane conductance). Thus, the results in Figure
305 5 can be described by three distinct steps: 1) ultrasound rapidly increases membrane capacitance
306 (C) at the onset of the ultrasound pulse, which causes the membrane voltage (V) to become less
307 negative (due to an increase in the denominator in the equation V=Q/C, where Q is the negative
308 total charge on the membrane); 2) ionic currents then slowly change the membrane voltage to a
309 steady-state value determined by the total ionic current (one or more ion channels having been

310 affected by ultrasound) resulting in membrane hyperpolarization; 3) at the offset of the ultrasound
311 pulse, capacitance rapidly relaxes back to its initial value, producing a transient decrease in
312 membrane voltage, through essentially the same mechanism as in step 1. We investigate the
313 physical basis of these capacitance changes and their relationship to the effects of ultrasound on
314 excitability further below, but one point worth mentioning here is that the change in capacitance
315 is too small for its effect on the rate of membrane charging (less than 1% change in membrane
316 time constant) to have a significant effect on excitability in and of itself.
317
318 *The K2P channel hypothesis.* What ion channels might be responsible for the effects of ultrasound
319 on excitability and resting membrane potential? A compelling hypothesis—able to explain all of
320 our data—is that ultrasound activates a non-inactivating, voltage-insensitive potassium channel,
321 such as members of the K2P potassium channel family. A primary reason for suspecting such
322 channels is that the effects of ultrasound are similar regardless of whether ultrasound is presented
323 500 ms before or 1 s after the start of the current step (compare Figures 2 and 3), consistent with
324 the idea that ultrasound affects a channel whose activation/inactivation status does not change
325 during that time period. Related to this point, the effects of ultrasound are not diminished by
326 repetitive, high-frequency action potential firing (for example, in Figure 4D effects of ultrasound
327 are clearly present throughout the entire 20-Hz, 10-spike train). Further, a striking feature of the
328 effects of ultrasound on spike intervals is that ultrasound always increases the latency to the first
329 spike (Figure 4B-D), regardless of the input current or intrinsic spike frequency. This observation
330 is also consistent with the idea that ultrasound affects a voltage-insensitive channel, whose
331 activation is not modulated by input current or spike frequency.
332 CA1 pyramidal neurons express a variety of K2P channel subunits. Expression of TASK-
333 1 and TASK-3, TREK-1 and TREK-2, TRAAK, and TWIK has been shown at the mRNA level
334 (Talley et al., 2001), while expression at the protein level has been shown has been shown for
335 TASK-3 in CA1 pyramidal neurons specifically (Marinc et al., 2014), and for TRAAK throughout

336 the central nervous system (Brohawn et al., 2019). In addition, functional expression of TASK-like
337 currents has been shown in CA1 pyramidal neurons using patch-clamp recording (Taverna et al.,
338 2005). TREK and TRAAK channels are particularly interesting in the present context since they
339 are exceptionally sensitive to mechanical force and to increases in temperature between
340 approximately 20 and 40°C (Maingret et al., 2000; Kang et al., 2005). Thus, TREK and TRAAK
341 channels are responsive to the two leading candidate mechanisms by which ultrasound at 43
342 MHz could modulate ion channel activity.

343 Activation of K2P channels by ultrasound could account for all of the neurophysiological
344 effects of ultrasound described so far: hyperpolarization of resting membrane potential; inhibition
345 of action potential firing in response to near-threshold current injections; and—although this last
346 point may seem counter-intuitive—potentiation of action potential firing at high firing frequencies.
347 Hyperpolarization of resting membrane potential by increased outward K^+ current is
348 straightforward, as is the idea that K^+ current can inhibit firing, but K^+ current can also potentiate
349 firing by its effects on action potential repolarization and afterhyperpolarization (AHP). By
350 accelerating the rate of membrane repolarization following the peak of an action potential (thereby
351 reducing action potential width) K^+ current can reduce inactivation of voltage-dependent Na^+
352 channels during the action potential, and by increasing the depth of the AHP, it can accelerate
353 the voltage-dependent recovery of Na_V channels from inactivation. Both of these effects would
354 tend to increase the population of Na_V channels available for activation in response to depolarizing
355 current and would increase the maximum action potential firing frequency, as we in fact see in
356 response to ultrasound (Figures 2 and 3). This mechanism is well-known and widespread in
357 neurophysiology, with several K^+ channels, including both K2P channels and voltage -
358 dependent K^+ channels (K_V channels), having been shown to facilitate high frequency firing (Lien
359 and Jonas, 2003; Brickley et al., 2007; Gu et al., 2007; Liu and Bean, 2014; Kanda et al., 2019).
360 The idea that the potentiation of firing by ultrasound is due to effects on action-potential
361 repolarization and AHP is supported by the results in Figure 4D. For neurons firing at an average

362 firing frequency of 20 Hz in the absence of ultrasound, ultrasound increases the latency to the
363 first spike, while it decreases the intervals between all subsequent spikes. The lack of a
364 potentiating effect on the first spike, despite the otherwise strongly potentiating effects of
365 ultrasound, indicates that the potentiating effect acts through a process (such as action-potential
366 repolarization and afterhyperpolarization) that occurs *after* the initiation of the first action potential.
367 The idea that ultrasound can potentiate firing by activating K^+ current makes specific predictions
368 about the effects of ultrasound on action potential waveform: ultrasound should accelerate
369 repolarization, decrease action potential width, and increase the depth of the
370 afterhyperpolarization.
371
372 *Effects of ultrasound on action-potential waveform.* To test the idea that potentiation of firing by
373 ultrasound is due to activation of K^+ channels, we examined the effects of ultrasound on action-
374 potential waveform in our recordings. The effects of ultrasound on action-potential waveform are
375 consistent with the idea that ultrasound facilitates high-frequency firing by accelerating action-
376 potential repolarization. Figure 6A-F shows the effect of ultrasound applied 500 ms before the
377 start of the current step on action-potential width for cells firing at average frequencies of 5, 10,
378 and 20 Hz. (Ultrasound also had effects on action-potential height, although these were less
379 pronounced than the effects on width; effects on height are detailed in Supplemental Figure 3.)
380 Ultrasound decreased action-potential width for every action potential at all firing frequencies. As
381 shown in Figure 6G-H, ultrasound also decreased action-potential width when applied 1 s after
382 the start of a current step, again indicating that the channels responsible for these effects continue
383 to influence firing frequency and remain responsive to ultrasound throughout sustained
384 depolarizing current steps.
385 The effects of ultrasound on action-potential width tended to counteract the broadening of
386 action-potential width that occurs during high-frequency firing. Figure 7 plots action potential width
387 as a function of action potential number and input current for the control and ultrasound conditions.

388 In the control condition, there are dramatic differences in width between the first action potential
389 and subsequent action potentials at high input currents, while in the ultrasound condition these
390 differences are much less pronounced. To quantify this effect, we measured the difference in
391 width between the first and third, first and fifth, and first and last action potentials during the
392 ultrasound stimulus, in response to a +450 pA current step for the control and ultrasound
393 conditions. These differences (mean ± SEM, control vs. ultrasound, N = 9) were 2.6 ± 0.9 vs. 0.7
394 ± 0.1 ms, 1.5 ± 0.1 vs. 0.5 ± 0.1 ms, and 1.2 ± 0.2 vs 0.5 ± 0.1 ms for the third, fifth, and last action
395 potentials (P = 0.064, 1.4 x 10^{-5}, and 0.0013, paired, two-tailed Student's t-test). One plausible
396 interpretation of this result is that K2P channels activated by ultrasound take over the role of K_V
397 channels that would otherwise contribute to action-potential repolarization. Since time-dependent
398 activation and inactivation of K_V channels causes action-potential broadening during repetitive
399 firing (Giese et al., 1998; Shao et al., 1999; Yue and Yaari, 2004; Kim et al., 2005; Gu et al.,
400 2007), replacement of these channels by K2P channels lacking time-dependent activation and
401 inactivation would reduce time- and frequency-dependent action potential broadening.

402 Although the effects of ultrasound on action-potential widths are predominantly due to
403 acceleration of the repolarization phase, we also noted effects on the rising phase of the action
404 potential. These effects are readily apparent in the first derivative of membrane voltage during the
405 action potential (Figure 8A) or in action potential phase plots (plots of the first derivative of voltage
406 versus voltage, Figure 8B). In fact, the maximum rates of voltage rise and fall during the action
407 potential were both consistently increased by ultrasound throughout a spike train (Figure 8C-D).
408 The effect on the falling phase is to be expected based on the observed decrease in spike width
409 and the hypothesis that ultrasound activates K2P channels. The effect on the rising phase is also
410 consistent with this hypothesis, as activation of K2P leading to reduced Na_V channel inactivation
411 would increase the number of Na_V channels available to activate during the rising phase of the
412 action potential.

413 In addition to effects of ultrasound on the rising and falling phases of the action potential,
414 we also found effects on the AHP. To quantify these effects, we measured the voltage minimum
415 between action potentials during repetitive firing. Because measurements of this parameter are
416 very sensitive to changes in resting membrane voltage and series resistance that can occur over
417 long recording times, we compared voltage minimums before, during, and after ultrasound
418 application within the same voltage trace (Figure 9A-B) and made a similar comparison for control
419 recordings. We performed these comparisons for ultrasound applied 1 s after the start of a current,
420 for cells firing at an average frequency of 5 Hz in the control condition. This firing frequency is
421 near the transition region between the inhibitory and potentiating effects of ultrasound on spike
422 frequency, such that the spike frequency is similar for the control and ultrasound conditions,
423 allowing us to compare a similar number of interspike voltage minima for the control and
424 ultrasound conditions (Figure 9C). This analysis demonstrates that the depth of the AHP is greater
425 during the ultrasound application than before or after it, or during the same time windows for the
426 control condition. Together with the effects of ultrasound on spike waveform (Figure 6), this result
427 supports the idea that ultrasound activates a sustained outward current, which limits Na_V channel
428 inactivation and thereby potentiates high-frequency firing. Removal of Na_V channel inactivation
429 by membrane hyperpolarization also explains how ultrasound can rescue spiking in neurons that
430 have entered a refractory state due to accumulation of Na_V channel inactivation (Figure 3C,
431 *bottom right*).
432
433 *Physical mechanism of neuromodulation by high-frequency ultrasound.* The idea that ultrasound
434 acts on K2P channels is also consistent with the physical effects of ultrasound on biological tissue.
435 At 43 MHz, two plausible mechanisms through which ultrasound might modulate the activity of
436 ion channels are heating and mechanical stress due to acoustic radiation force. Absorption of
437 acoustic energy by biological tissue as heat can increase its temperature, with effects on ion
438 channel gating and all other biological reactions. Absorption also results in attenuation of

439 ultrasound intensity as the wave propagates, creating spatial gradients in intensity that give rise
440 to radiation force, which in turn produces tissue displacement and strain. At the microscopic scale,
441 this displacement and strain may involve increased tension in the cell membrane, cytoskeleton,
442 and extracellular matrix, all of which may affect excitability through mechanical effects on ion
443 channel proteins. Among the K2P channels that may be expressed by CA1 pyramidal cells, TREK
444 and TRAAK channels are especially sensitive to thermal and mechanical stimuli.

445 To gain further insight into these physical mechanisms, we performed finite-element
446 simulations of the effects of ultrasound on brain slices in the context of our experimental set-up.
447 The simulated spatial profiles of ultrasound-induced heating and macroscopic tissue
448 displacement in response to radiation force are shown in Figure 10A-B. Notably, the spatial
449 profiles of heating and displacement effects are significantly wider than the 90-micron diameter
450 of the focal volume of the ultrasound beam, with significant heating and displacement occurring
451 several hundreds of microns away from the beam axis (Figure 10C). This is an important result
452 because the thermo- and mechanosensitive K2P channels TREK-1 and TRAAK are expressed
453 at high density at the nodes of Ranvier of vertebrate neurons (Brohawn et al., 2019; Kanda et al.,
454 2019). The first node of Ranvier is located approximately 100 microns from the axon initial
455 segment (Kole, 2011). In our experiments, the soma of the patched neuron is located
456 approximately on the axis of the ultrasound beam (see *Materials and Methods*) so the first node
457 of Ranvier is probably within the region of the tissue exposed to thermal and mechanical effects
458 of ultrasound. Axonal K^+ channels play important roles in regulating excitability (Shah et al., 2008;
459 Kole, 2011; Kanda et al., 2019). It is therefore plausible that a subpopulation of TREK-1 or TRAAK
460 channels at the nodes of Ranvier could contribute to the neurophysiological effects of ultrasound.
461 The magnitude of the temperature change is also consistent with a thermal mechanism for the
462 effects of ultrasound. The maximum temperature change in the simulation is 1.3 C; temperature
463 changes of this size have previously been shown to affect neural excitability (Owen et al., 2019).
464 The maximum value of the simulated displacement (1.7 microns) is similar to the displacement

465 measured in the retina during ultrasound neuromodulation with stimulus parameters similar to
466 those used here (Menz et al., 2019).

467 It is instructive to consider the amplitude and time course of the membrane capacitance
468 change in response to ultrasound (Figure 5) in the context of possible thermal and mechanical
469 mechanisms. As described above (under *Effects of ultrasound on resting membrane potential*),
470 the capacitance change in response to ultrasound is fast relative to the membrane time constant,
471 so we can assume that the total charge on the membrane is constant during the initial transient
472 depolarization in response to ultrasound (Figure 5A, *left arrow*). In other words, the numerator in
473 the equation V = Q/C is constant, so for small changes in voltage the relative change in voltage
474 is approximately inversely proportional to the relative change in capacitance. Empirically,
475 membrane capacitance increases by approximately 1% per degree C (Taylor, 1965). This is
476 consistent with the size of the simulated temperature rise (peak simulated temperature rise of
477 1.3°C compared with the measured amplitude of the initial decrease in voltage of 0.7 ± 0.1%).
478 However, the time course of the temperature rise (Figure 10D) is much slower than the time
479 course of the voltage transient (which again, assuming constant Q, is identical to the time course
480 of the capacitance change). The time course of the change in resting membrane potential (173 ±
481 18 ms, Figure 5), however, parallels that of the temperature rise. (A capacitance change on the
482 time course of the simulated temperature rise would not have a significant effect on the membrane
483 voltage, as it would be counteracted by ionic currents.) Thus, the simulated ultrasound heating
484 results strongly suggest that ultrasound affects action-potential firing in our experiments at least
485 in part through a thermal effect on ion channels, but do not explain the presence of the capacitive
486 transients.

487 We considered whether the time course of the capacitive transients could instead be
488 explained by the dynamics of the tissue mechanical response to acoustic radiation force. We
489 sought to determine whether, having already modeled the static displacement of the tissue, we
490 could, without retroactively changing any of the tissue material properties, obtain a time course

491 for tissue displacement similar to that of the capacitive transients using a simple viscoelastic
492 model with reasonable tissue viscous properties (see *Materials and Methods*). We found that this
493 could be achieved using a shear viscosity (m) of 1 Pa·s (Figure 10E). Since the tissue is
494 essentially incompressible in our model (Poisson's ratio (n) = 0.4998), this is equivalent to a
495 relaxation time of $2m\cdot(1+n)/E$ = 6 ms (where E is Young's modulus). Biological tissue is a highly
496 heterogeneous material that displays a variety of active and passive mechanical responses to
497 force, spanning time scales from milliseconds to hours (Ricca et al., 2013), and as a result its
498 viscous properties are highly sensitive to the time scale of the measurement and even complex
499 viscoelastic models encompassing multiple relaxation times may not fully describe the
500 viscoelastic behavior of tissue. Nonetheless, the shear viscosity/relaxation time in our model is
501 reasonable for a soft, gel-like material, and is comparable to fast relaxation times observed
502 experimentally in brain tissue (Arbogast and Margulies, 1999; Abolfathi et al., 2009; Rashid et al.,
503 2012, 2013). Moreover, the simulated time course of displacement is consistent with experimental
504 measurements of the tissue displacement in response to ultrasound at 43 MHz and 40 W/cm^2 in
505 the salamander retina, which was found to be complete in less than 10 ms (Menz et al., 2019).
506 We can therefore make the reasonable assumption that the capacitive transients are due
507 to a mechanical effect on membrane properties, and we can estimate the size of the potential ion-
508 channel gating effects that would occur as a result of this mechanical effect. The capacitance of
509 a lipid bilayer membrane is given by $C = \varepsilon\cdot\varepsilon_0\cdot A/L$, where ε is the dielectric constant of the
510 hydrophobic core of the lipid bilayer, ε_0 is the permittivity (polarizability) of free space, A is
511 membrane area, and L is the thickness of the hydrophobic core of the membrane. For small
512 strains like those under consideration here, lipid bilayer membranes can be considered
513 incompressible, such that a 1% increase in capacitance corresponds to a 0.5% increase in area
514 and a 0.5% decrease in thickness (White and Thompson, 1973; Alvarez and Latorre, 1978). An
515 increase in membrane area can be converted to an increase in membrane tension (γ) according

516 to $\gamma = \Delta A \cdot K_A$, where ΔA is the relative change in area and K_A is the area elastic constant of the
517 membrane. Area elastic constants measured for lipid membranes are on the order of 100's of
518 mN/m (Evans et al., 1976; Kwok and Evans, 1981; Needham and Nunn, 1990). If the capacitance
519 transients are due to membrane strain, the resulting membrane tension is on the order of a few
520 0.1 mN/n to a few mN/m. These values are similar to the tension thresholds for activation of
521 mechanosensitive K2P channels (estimated as 0.5-4 mN/m for activation of TREK-1 and TRAAK
522 (Brohawn et al., 2014)), which are low relative to other known mammalian mechanosensitive
523 channels. Notably, a recent *in vivo* ultrasound neuromodulation study of the murine sciatic nerve
524 at 4 MHz, found that tissue displacement *in vivo* was highly correlated with the neuromodulation
525 effects (Lee et al., 2020). Nonetheless, additional data or theoretical advances would be required
526 to firmly associate these capacitive transients with changes in membrane tension. If such an
527 association could be made, it would provide strong evidence that ultrasound modulates action
528 potential firing through mechanical effects of radiation force in our experiments. At present, our
529 results do not rule out this idea, but the case for mechanical effects remains speculative, while
530 the role of thermal effects seems highly plausible. Nonetheless, our simulation results support the
531 conclusion that both inhibitory and excitatory effects of high-frequency ultrasound on action-
532 potential firing are due to activation of thermo- and mechanosensitive K2P channels.
533

534 **DISCUSSION**

535 To summarize, the neurophysiological effects of ultrasound that we have described here can all
536 be explained by activation of a sustained outward current. We argue that the molecular basis of
537 this outward current is most likely one or more of the K2P channels expressed by CA1 pyramidal
538 neurons. Although a variety of voltage-dependent K+ currents shape the action-potential
539 waveform and regulate excitability in these neurons, several arguments suggest that K2P
540 channels are the molecular basis of the ultrasound-activated outward conductance. First, the K2P
541 channels TREK and TRAAK, being strongly mechanosensitive and thermosensitive, have

542 biophysical properties that make them especially sensitive to physical effects of ultrasound.
543 Second, the fact that ultrasound has similar effects on firing frequency whether it is applied 500
544 ms before or 1 s after the start of a current step suggests that ultrasound affects firing through a
545 channel whose properties are not strongly modulated by voltage. Finally, the neurophysiological
546 effects of ultrasound are, strikingly, essentially the opposite of those caused by knock-out of
547 TASK-3 channels in cerebellar granule neurons (Brickley et al., 2007), which increased excitability
548 at low input currents, but decreased excitability at high input currents and led to failure of
549 sustained high-frequency firing. In addition, knock-out of TASK-2 decreased the maximum firing
550 frequency and decreased action-potential height while increasing action potential width. TREK-1
551 and TRAAK channels are also necessary for high frequency firing at the nodes of Ranvier of
552 afferent neurons (Kanda et al., 2019).

553 Ultrasound neuromodulation has been studied in vertebrate axon preparations, where it
554 has generally been found that ultrasound inhibits action-potential conduction, with the effect
555 specifically attributed to heating in some cases (Young and Henneman, 1961; Mihran et al., 1990;
556 Tsui et al., 2005; Colucci et al., 2009). These results are consistent with the idea that activation
557 of K2P channels by ultrasound can inhibit action potential firing, but it would be worthwhile to
558 revisit these experiments to see whether the bidirectional, spike-frequency-dependent effect that
559 we observe is also present in such preparations. Our results also suggest an approach to
560 ultrasound neuromodulation in which action potential propagation is the locus of neuromodulation,
561 targeting white-matter tracts instead of soma-dense gray matter. The idea that ultrasound-
562 activated K^+ currents can both inhibit and potentiate firing might also help explain why ultrasound
563 can both inhibit and potentiate neural activity *in vivo* (Min et al., 2011).

564 Although activation of K2P channels is sufficient to explain our results, we do not rule out
565 the possibility that ultrasound affects other channels in addition to K2P's; indeed, we think it is
566 likely that ultrasound does affect other channels to some extent. All ion-channel gating reactions
567 are sensitive to temperature, with typical Q10 values of ~3, such that their rates would be

568 expected to increase by about 10% based on the temperature changes in our simulations (Hille,
569 2001). Mechanical effects of radiation force could also affect channels besides K2P channels.
570 The mechanically gated channel Piezo2 is expressed in a subset of CA1 pyramidal neurons
571 (Wang and Hamill, 2020). In addition, most ion channels and membrane proteins, while not
572 functioning physiologically as mechanoreceptors, are sensitive to mechanical stimuli to some
573 extent, either through the energetics of their interactions with hydrophobic core of the lipid bilayer
574 or through mechanical interactions with the cytoskeleton or extracellular matrix. In fact, gating of
575 voltage-dependent Na^+, K^+, and Ca^{2+} channels can be modulated by membrane stretch in
576 membrane patches (Calabrese et al., 2002; Tabarean and Morris, 2002; Laitko and Morris, 2004;
577 Morris and Juranka, 2007; Beyder et al., 2010). However, we previously were unable to detect
578 any mechanical modulation of heterologously expressed NaV1.2 channels by ultrasound at 43
579 MHz and 90 W/cm^2 under conditions where ultrasound activated the mammalian
580 mechanoreceptor channel Piezo1 (Prieto et al., 2018). Neural Na_V channels and KCNQ channels
581 interact with the periodic actin cytoskeleton of axons through spectrin and ankyrin-G at the axon
582 initial segment and nodes of Ranvier and (Zhou et al., 1998; Pan et al., 2006; Leterrier, 2018),
583 suggesting that they may be sensitive to modulation by cytoskeletal tension. The concentration
584 of TREK-1 and TRAAK channels at the nodes of Ranvier suggest that some similar interaction
585 with the cytoskeleton may be involved in the localization of these channels, although this has not
586 been demonstrated, and the intracellular domains that would facilitate such interactions are
587 relatively small in K2P channels.

588 It is well established that high-intensity light at infrared and shorter wavelengths can
589 modulate neural activity through tissue heating. As a general principle, thermal neuromodulation
590 effects in response to optical stimulation would be expected to be very similar to thermal
591 neuromodulation effects caused by ultrasound, and studies of optical neuromodulation could
592 therefore provide useful guidance in interpreting our results. However, optically based thermal
593 neuromodulation experiments are highly heterogeneous in terms of the neuromodulation effect,

594 the temperature rise required to produce the effect, and the mechanistic interpretation of the
595 results (Wells et al., 2007; Richter et al., 2011; Shapiro et al., 2012; Duke et al., 2013; Walsh et
596 al., 2016; Lothet et al., 2017; Paris et al., 2017; Owen et al., 2019; Zhu et al., 2019), so their
597 usefulness is limited in this respect. Both inhibition and potentiation of firing have been reported,
598 and the increase in temperature has varied considerably, ranging from less than 1 C to 10's of
599 degrees C. The temperature rise in our simulations is on the low end of this range. However, it
600 has been proposed that spatial or temporal gradients in temperature, rather than the absolute
601 temperature change, may determine the response to thermal stimuli (Wells et al., 2007; Paris et
602 al., 2017). In addition, heating can cause phase changes in lipid bilayers, which have been shown
603 to modulate ion channel activity (Seeger et al., 2010); in this case, the response to heating would
604 also depend critically on the initial temperature. Interestingly, a recent study demonstrated
605 inhibition of firing by small (2°C or less) increases in temperature in several different types of
606 neurons, but *not* in CA1 pyramidal neurons (Owen et al., 2019). These effects were attributed to
607 inward rectifier (K_{ir}) potassium channels, which are not expressed in CA1 pyramidal neurons.
608 However, our results suggest that the lack of an effect in pyramidal neurons could also be
609 explained if the experiments were performed at a point on the f-i curve where competing inhibitory
610 and excitatory effects of heat-activated K^+ current result in no net effect on firing frequency. A
611 recent *in vivo* ultrasound neuromodulation study in a rat model using ultrasound at 3.2 MHz with
612 exceptionally long ultrasound exposure times (10's of seconds; see below for a more general
613 discussion of *in vivo* ultrasound neuromodulation studies) also found that inhibition could be
614 produced by ultrasound-induced temperature rises of 2°C or less (Darrow et al., 2019), consistent
615 with this result and our results.

616 Finally, a critical question—to which we cannot yet provide a definitive answer—is whether
617 the mechanisms underlying the neuromodulatory effects of ultrasound are the same in our
618 experiments and in *in vivo* experiments using low frequencies. Two results that strongly argue
619 against similar mechanisms are the apparent frequency-dependence of neuromodulation in *in*

620 *vivo* experiments, and the much lower intensities that have been reported to cause
621 neuromodulatory effects in some low-frequency, *in vivo* experiments as compared with our
622 results. In an *in vivo* mouse model of ultrasound neuromodulation, it was determined that the
623 efficacy of neuromodulation decreased with increasing frequency over the range 0.25-2.9 MHz
624 (King et al., 2013; Ye et al., 2016). This frequency dependence is the opposite of what would be
625 expected for either a thermal or radiation force mechanism, since both of these are proportional
626 to the ultrasound attenuation coefficient, which in tissue is proportional to frequency raised to the
627 power of ~1.1 (Hand, 1998). In contrast, Menz et al. (2019) found that the efficacy of
628 neuromodulation increases with frequency over the range 1.9-43 MHz in the retina *in vitro*, a thin
629 neural tissue preparation similar to the one used in our experiments. However, they proposed a
630 model to explain this discrepancy. Lower ultrasound frequencies generally result in a larger
631 stimulated tissue volume, which could translate into a more effective stimulus for certain
632 structures of circuit-level neural connectivity, despite a weaker effect of low-frequency ultrasound
633 at the level of an individual cell. (The model was presented in the context of a radiation force
634 mechanism, but the same principle could apply for a thermal mechanism). The idea that circuit-
635 level mechanisms can amplify the response to ultrasound is supported by comparison of our
636 results with the response to ultrasound in the retina at 43 MHz. In the retina, potentiation of action-
637 potential firing by ultrasound at 43 MHz saturates at 10 W/cm^2, as measured at the population
638 level in an intact, active neural circuit. Although we have not performed a detailed investigation of
639 the intensity dependence, we find that a much higher intensity, 50 W/cm^2, produces relatively
640 moderate effects on excitability in single cells in the absence of significant network activity.

641 Such considerations may mitigate frequency-dependence as an argument against similar
642 physical mechanism for neuromodulation by high- and low-frequency ultrasound. The other major
643 argument against similar mechanisms for high and low frequencies is the difference in the size of
644 the potential thermal of radiation force effects at different intensities and frequencies. One point
645 specific to the K2P channel hypothesis is worth mentioning in this context. The midpoints of the

646 temperature-activation curves for TREK and TRAAK channels are near 37°C (in other words,
647 near body temperature in mammals) so that the increase in K2P current in response to increased
648 temperature is near maximal at physiological temperature (Maingret et al., 2000; Kang et al.,
649 2005), whereas our experiments were performed at room temperature (21-23°C). Room
650 temperature is near the threshold for temperature activation of these channels, such that they are
651 mainly inactive at room temperature in the absence of other stimuli such as membrane stretch,
652 lipid agonists, or acidic pH.

653 In conclusion, our results demonstrate that high-frequency ultrasound is a viable and
654 promising modality for neuromodulation applications where frequency is not limited by
655 transmission through the skull, and our insights into the common molecular mechanisms
656 underlying both inhibitory and excitatory effects of high-frequency ultrasound pave the way for
657 rational design and optimization of neuromodulation protocols to consistently produce either
658 inhibitory or excitatory effects.

659

660 **ACKNOWLEDGMENTS**

661 We thank the PIs and members of the Baccus, Butts-Pauly and Huguenard laboratories for helpful
662 discussions. We thank Mike Menz and Stephen Baccus for critically reading the manuscript. We
663 thank Marianna Kiraly, Dong Li, and Jason Clark for help with hippocampal slice preparation and
664 recording. We thank the Stephen Boxer lab for sharing their plasma cleaner.

665 This work was supported by NIH R01 EB019005 (M.M. and B.K.Y.), NIH BRAIN initiative R01
666 NS11215 (M.M. and B.K.Y.), NIH R01 MH111768 (D.M) and by the Harold and Leila Y. Mathers
667 Charitable Foundation (M.M and D.M).

668 The authors declare no competing financial interests.

669 **AUTHOR CONTRIBUTIONS**

Martin Prieto performed experiments, analyzed data, and wrote the manuscript. Martin Prieto and Kamyar Firouzi performed computational modeling. Merritt Maduke, Daniel Madison, and Butrus Khuri-Yakub supervised research. All authors contributed to the design and interpretation of experiments and edited and revised the manuscript.

Table 1. Values of Material Properties Used in Finite-Element Simulations.

	water	polystyrene	brain tissue
density (kg/m^3)	1000[a]	1040[b]	1007[c]
speed of sound (m/s)	1500[a]	2300[b]	1538[c]
attenuation coefficient at 43 MHz (neper/m)	46[d]	160[e]	253[f]
heat capacity (J/kg·K)	4180[a]	1200[g]	3500[h]
thermal conductivity (W/m·K)	0.6[a]	0.1[g]	0.5[h]
Young's modulus (Pa)	(not applicable)	10^9 [i]	500[j]
Poisson's ratio	(not applicable)	0.4[i]	0.4998[k]
shear viscosity (Pa·s)	(not applicable)	(not applicable)	1[l]

Sources for material properties are as follows: [a]standard value; [b]based on typical acoustic properties of plastics (Selfridge, 1985); [c]following Menz et al. (2019), based on (Thijssen et al., 1985); [d] (Company, 1965); [e]measured (Prieto et al., 2018); [f]following Menz et al. (2019), based on (de Korte et al., 1994); [g]based on typical thermal properties of plastics (Gaur and Wunderlich, 1982; Harper, 2006); [h]typical values for soft tissues (Hand, 1998); [i]based on typical mechanical properties of plastics (Harper, 2006); [j]Menz et al. (2019), from measurements of ultrasound-induced displacement in the retina; [k]tissue assumed to be incompressible for small deformations; [l]see text.

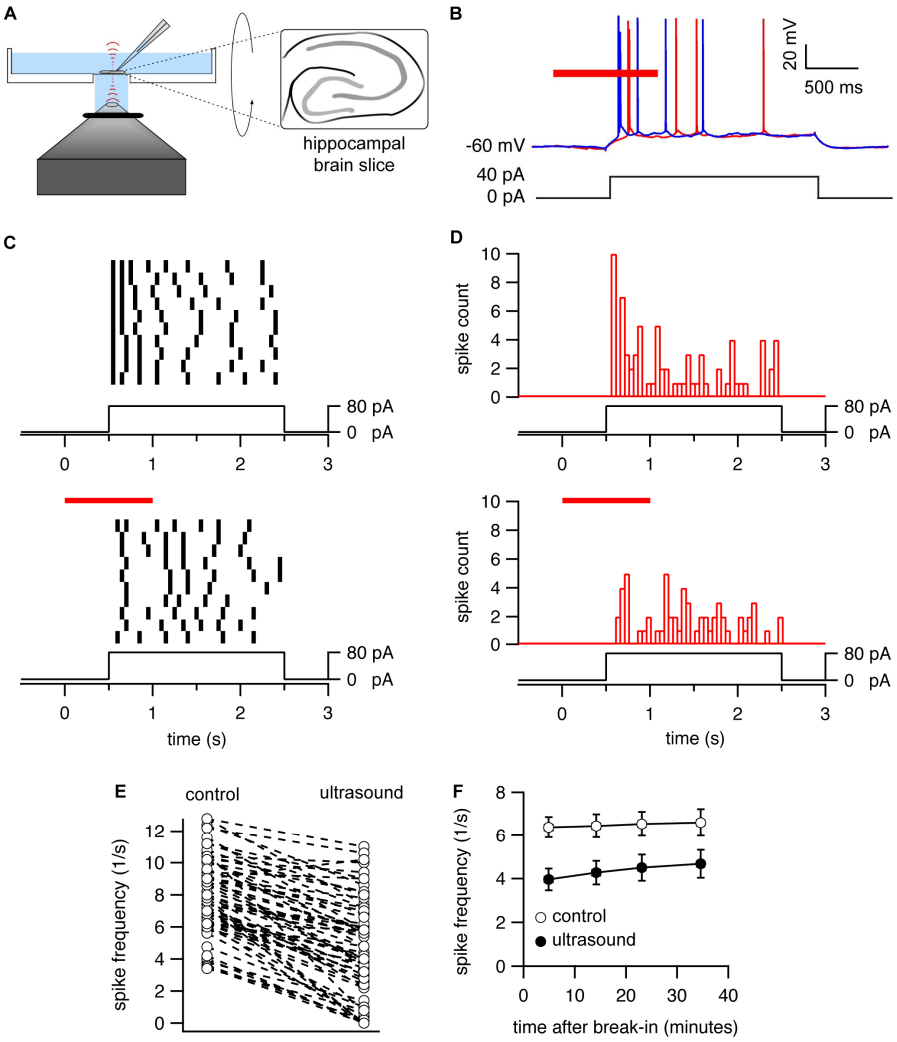

Figure 1. Consistent inhibition of action potential firing by high-frequency ultrasound. A. Diagram of experimental set-up. Ultrasound is applied to 500-micron hippocampal brain slices resting on a 25-micron film of polystyrene. The 43-MHz focused transducer is located below the experimental chamber, with ultrasound propagating perpendicular to the bottom of the recording chamber. **B.** Experimental protocol and example voltage traces showing inhibition of action potential firing by ultrasound. A 1-s, continuous-wave ultrasound pulse at 43 MHz and 50 W/cm^2 (*red bar*) is applied 500 ms before the start of a 2-s current injection. Voltage traces are shown in the presence (*red*) and absence (*blue*) of the ultrasound stimulus. **C.** Example raster plots showing a consistent effect of ultrasound on firing frequency. The results of twenty consecutive trials of the protocol in panel B, alternating between the control (*top*) and ultrasound (*bottom*) conditions, are shown. The voltage traces were divided into 50-ms bins; a solid black bin indicates that an action potential occurred within that particular time bin. Time is relative to the start of the ultrasound pulse. **D.** Spike-time histograms prepared by summing the ten trials for the control and ultrasound conditions from panel C. **E.** Summary of the effects of ultrasound for N = 66 cells. The average firing frequency during the first 500 ms of the current step is shown for the control and ultrasound conditions. **F.** Stability of the ultrasound response. Mean (±SEM, N = 10 cells) spike frequencies during the first 500 ms of a current step in the presence (*solid circles*) and absence (*open circles*) of ultrasound for the protocol shown in panel B, as a function of time relative to break-in (establishment of whole-cell recording configuration). Spike frequencies were measured at various time points between 0 and 10, 10 and 20, 20 and 30, and 30 and 40 minutes after break-in. The x-values represent the mean start time for the protocol to measure spike frequencies (which comprised 2 minutes of recording time). The amplitude of the current step was adjusted over time to maintain spiking behavior as close as possible to that at the start of the experiment.

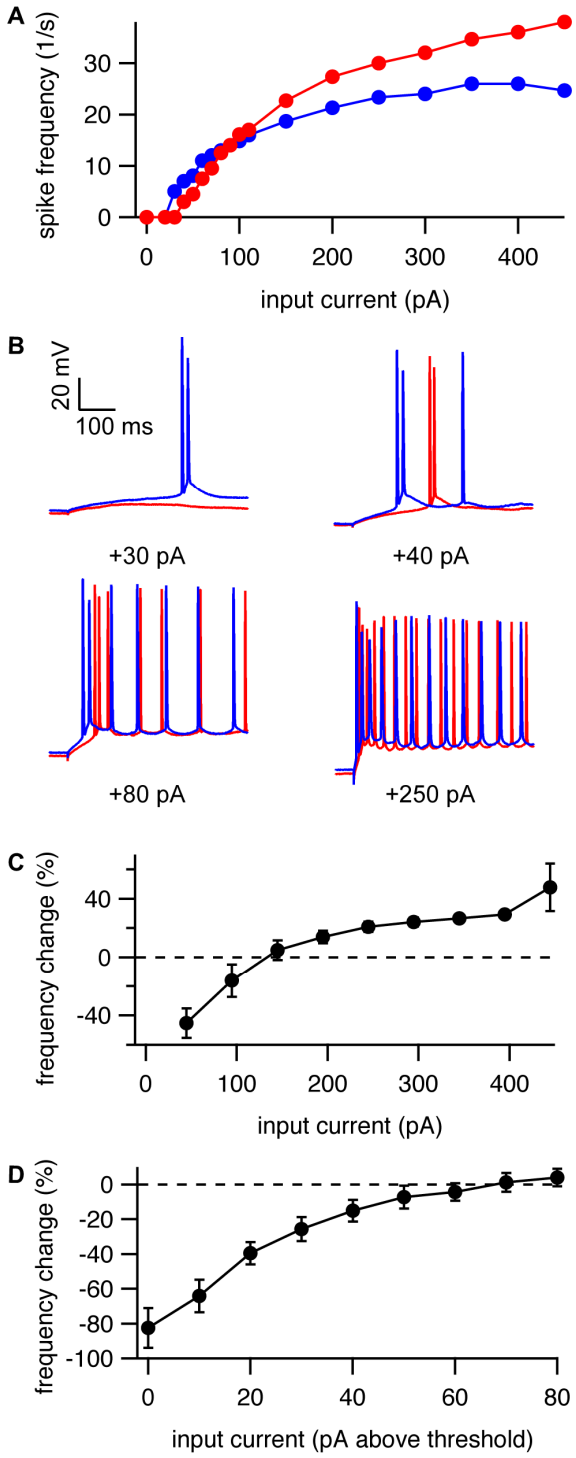

Figure 2. Ultrasound can inhibit or potentiate action-potential firing. A. Example frequency-input curve showing average firing frequency during the first 500 ms of a current step as a function of input current, with (*red*) and without (*blue*) a 1-s ultrasound pulse starting before 500 ms before the start of the current step. Each point represents the average of three trials on the same cell. **B.** Example voltage traces for the cell in A showing action potential firing during the first 500 ms of current steps to either +30, +40, +80, or +250 pA, with (*red*) and without (*blue*) ultrasound. **C.** Mean (±SEM, N = 9 cells) change in spike frequency in response to ultrasound as a function of input current. **D.** Inhibition is strongest near threshold. Mean (±SEM, N = 7 cells) change in spike frequency in response to ultrasound as a function of input current relative to the threshold current for action potential firing, for near-threshold currents.

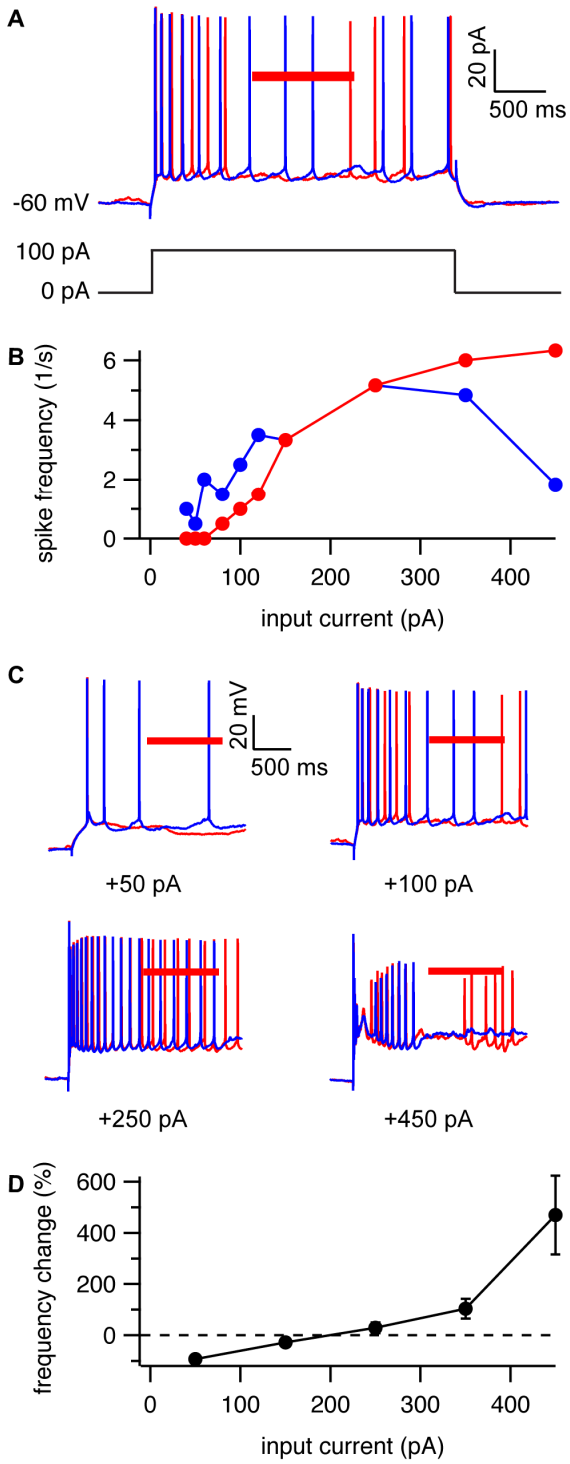

Figure 3. Ultrasound can also inhibit or potentiate action-potential firing when applied late in a current step. A. Experimental protocol and example voltage traces with (*red*) and without (*blue*) ultrasound. Ultrasound is applied 1 s after the start of a 3-s current step. **B.** Example frequency-input curve showing average firing frequency during the ultrasound application for the protocol in A (*red*) and during the same time window without ultrasound (*blue*), as a function of input current. Each point represents the average of three trials on one cell. **C.** Example voltage traces for the cell in B showing action potential firing during the ultrasound application (*red*) and during the same time window without ultrasound (*blue*) in response to current steps to either +50, +100, +250, or +450 pA. **D.** Mean (±SEM) change in spike frequency in response to ultrasound as a function of input current (N = 3 cells at +50 pA; N = 6 cells at all other input currents). (In 3 cells, the firing frequency at +50 pA was zero for both the control and ultrasound conditions).

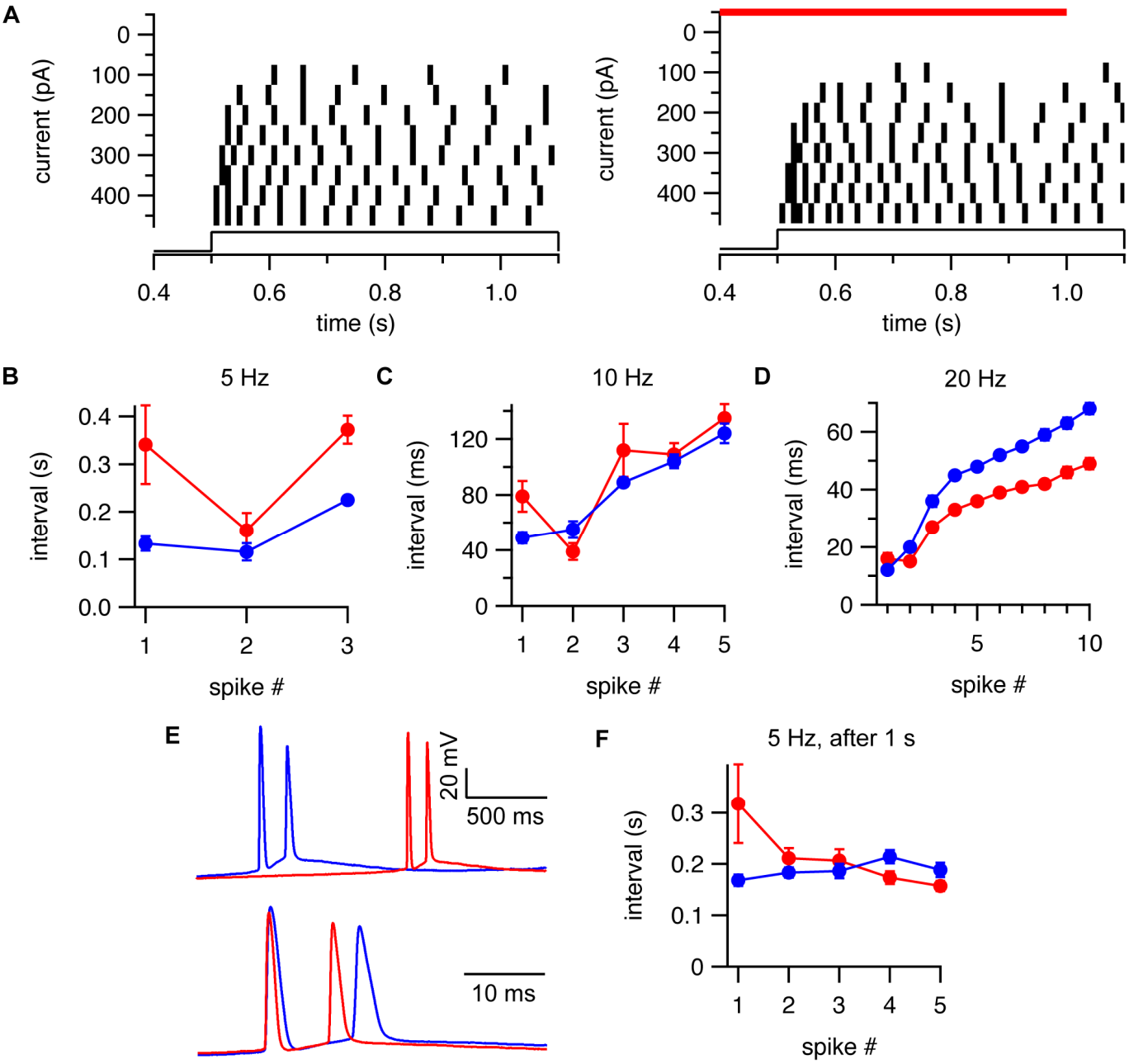

Figure 4. Effects of ultrasound on action potential timing. A-C. Mean (±SEM) intervals between the start of the current step and the first action potential, and between the first and second, and second and third, etc. action potentials, for cells firing at average frequencies of approximately 5 Hz (N = 13 cells), 10 Hz (N = 15 cells), and 20 Hz (N = 13 cells) during the first 500 ms of the current step, with (*red*) or without (*blue*) a 1-s ultrasound pulse starting 500 ms before the current step. The actual spike frequencies were 5.6 ± 0.1, 10.5 ± 0.2, and 20.4 ± 0.3 Hz, and the injected currents were 70 ± 7, 115 ± 9, and 292 ± 28 pA for the 5, 10, and 20 Hz conditions. **D.** Example voltage traces showing decreased interval between the first and second action potentials at low average firing frequency. The top panel shows the first two action potentials for the control (*blue*) and ultrasound (*red*) conditions. The bottom panel shows the same data, aligned to the action potential threshold on zoomed-in time scale. **E.** Same as A-C, for an currents was 183 ± 21 pA.

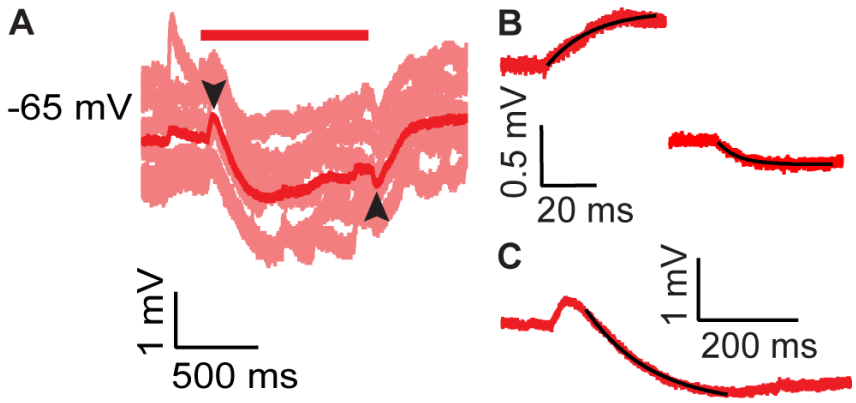

Figure 5. Effects of ultrasound on resting membrane potential and membrane capacitance. A. Six individual voltage traces (*pink*) and the average of these voltage traces (*red*) showing the effect of ultrasound at (*red bar*) on resting membrane potential. The *black arrows* indicate transients due to changes in membrane capacitance. **B.** Zoomed-in timescale showing the fast voltage transients (*black arrows* in A) for ultrasound onset (*top left*) and offset (*bottom right*). Exponential fits (*black lines*) to the rise and fall of the voltage transients give amplitudes and time constants of 0.45 mV and 16.3 ms for the onset and 0.22 mV and 6.7 ms for the offset, for the example shown; mean values (±SEM) were 0.41 ± 0.04 mV and 10.4 ± 1.2 ms for the onset and 0.35 ± 0.04 mv and 9.7 ± 1.7 ms for the offset (N = 15). No significant differences were found between the time constants (P = 0.73) or the amplitude (P = 0.087) of the transients (paired, two-tailed Student's t-tests) **C.** Slow membrane hyperpolarization in response to ultrasound from the average trace in panel A on a zoomed-in scale, along with an exponential fit (*black line*) to the initial hyperpolarization. The amplitude and time constant of the exponential fit were 1.55 mV and 132 ms for the example shown; mean values (±SEM) were 2.4 ± 0.3 mV and 173 ± 18 ms (N = 15).

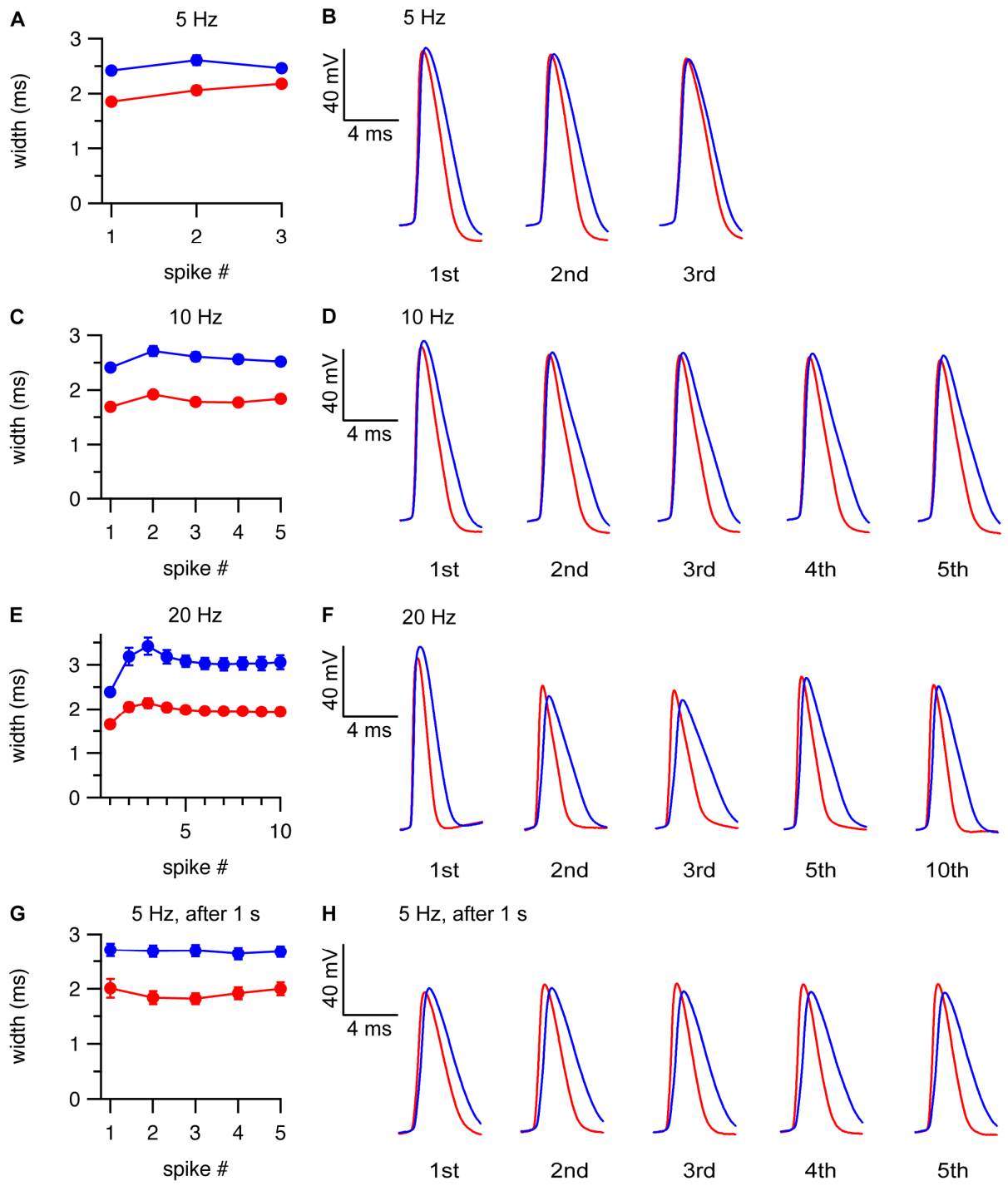

Figure 6. Ultrasound decreases action-potential width. A-B. Mean (±SEM, N = 13 cells) action potential-widths (A) and example action-potential waveforms aligned to the action-potential threshold (B) as function of action potential number in the presence (*red*) and absence (*blue*) of a 1-s ultrasound pulse starting 500 ms before the current step, for cells firing at an average firing frequency of approximately 5 Hz (as measured during the first 500 ms of the current step) in the control condition. **C-D.** As in A-B, but for cells firing at an average firing frequency of approximately 10 Hz in the control condition (N = 15). **E-F.** As in A-B, but for cells firing at an average firing frequency of approximately 20 Hz in the control condition (N = 13). **G-H.** As in A-B, but with ultrasound applied 1 s after the start of a 3-s current step, for cells firing at an average firing frequency of approximately 5 Hz in the control condition, with firing frequency determined in a 1-s window starting 1 s after the current step (corresponding to the time period of the ultrasound stimulus), and action potential number relative to the start of the ultrasound stimulus (N = 6).

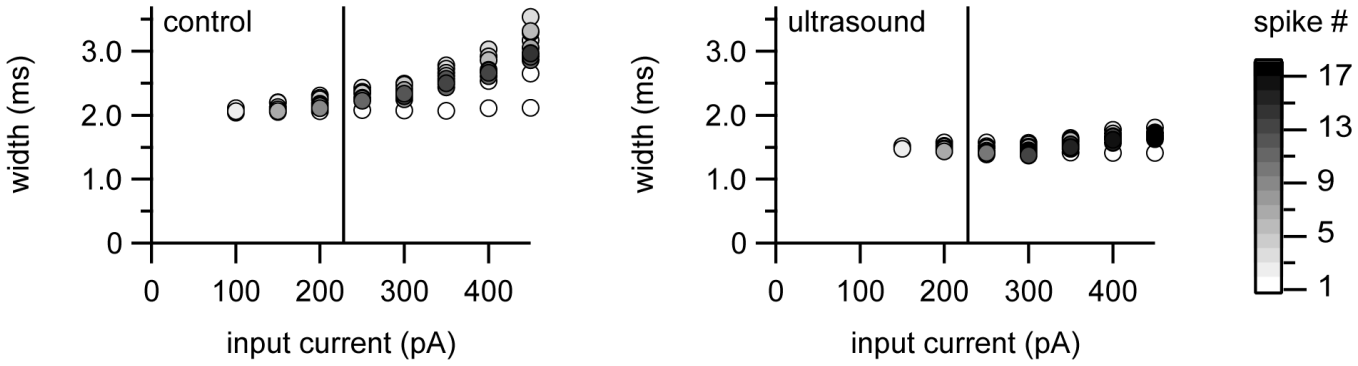

Figure 7. Ultrasound reduces action-potential broadening. Example data showing action-potential width as a function of action-potential number (indicated in *grayscale*, scale bar at far left) and input current level, for the first 500 ms of the current step, for currents from 0 to +450 pA in 50 pA steps, with (*right*) or without (*left*) a 1-s ultrasound pulse starting 500 ms before the current step. The vertical lines indicate the approximate location of the transition between inhibitory and potentiating effects of ultrasound.

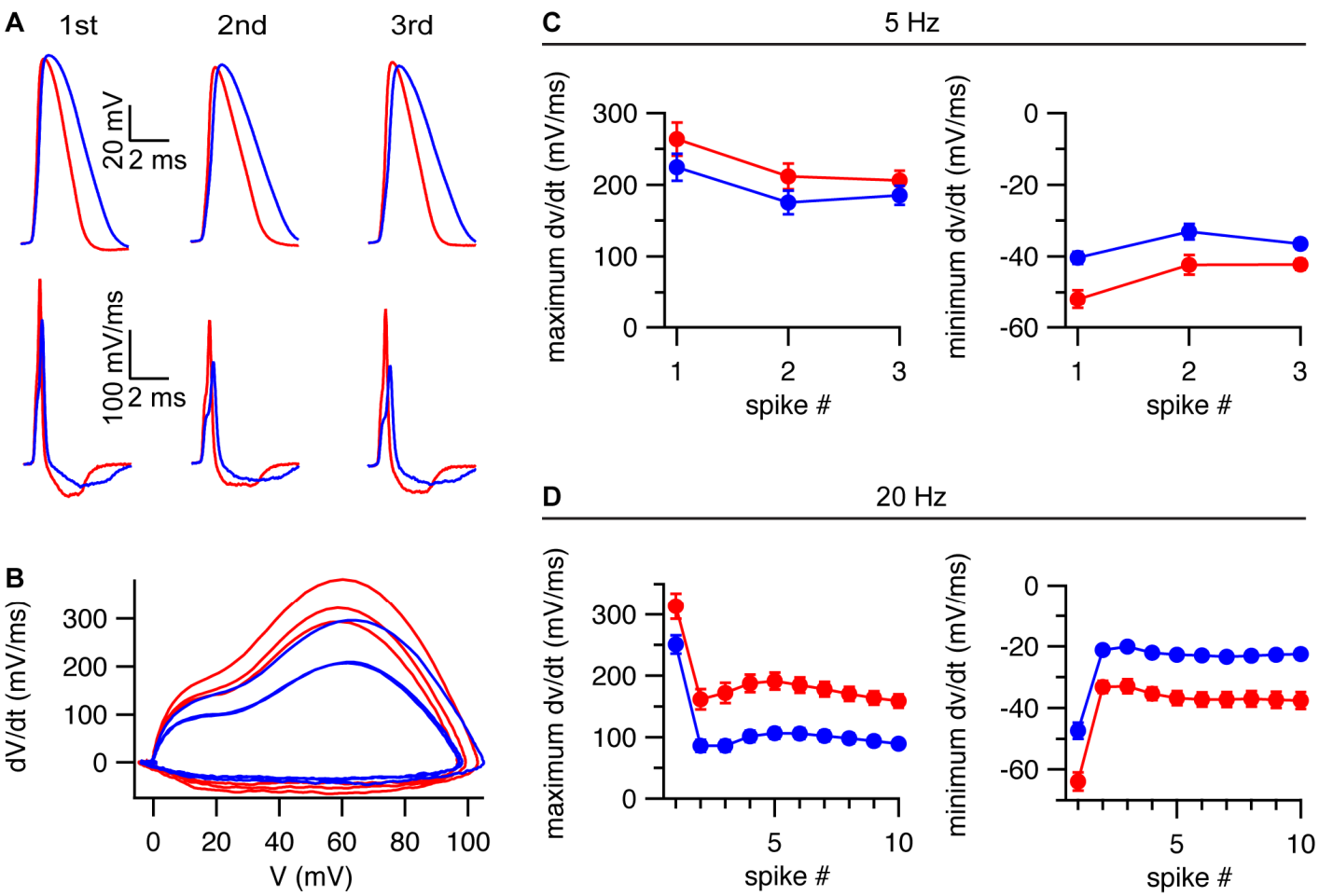

Figure 8. Effects of ultrasound on depolarization and repolarization rates. A. Example traces showing the membrane voltage (*top*) and its first derivative (*bottom*) for the first three action potentials in response to a +100 pA current step in the presence (*red*) and absence (*blue*) of a 1-s ultrasound pulse starting 500 ms before the current step, aligned to the action potential threshold. **B.** Phase plots for the action potentials shown in panel A. **C-D.** Maximum rates of depolarization (*left)* and repolarization (*right*) during the action potential (mean ± SEM, N = 13 cells), as a function of action potential number, in the presence (*red*) and absence (*blue*) of a 1-s ultrasound pulse starting 500 ms before the current step, for cells firing at an average firing frequency of 5 Hz (**C**) or 20 Hz (**D**) in the control condition.

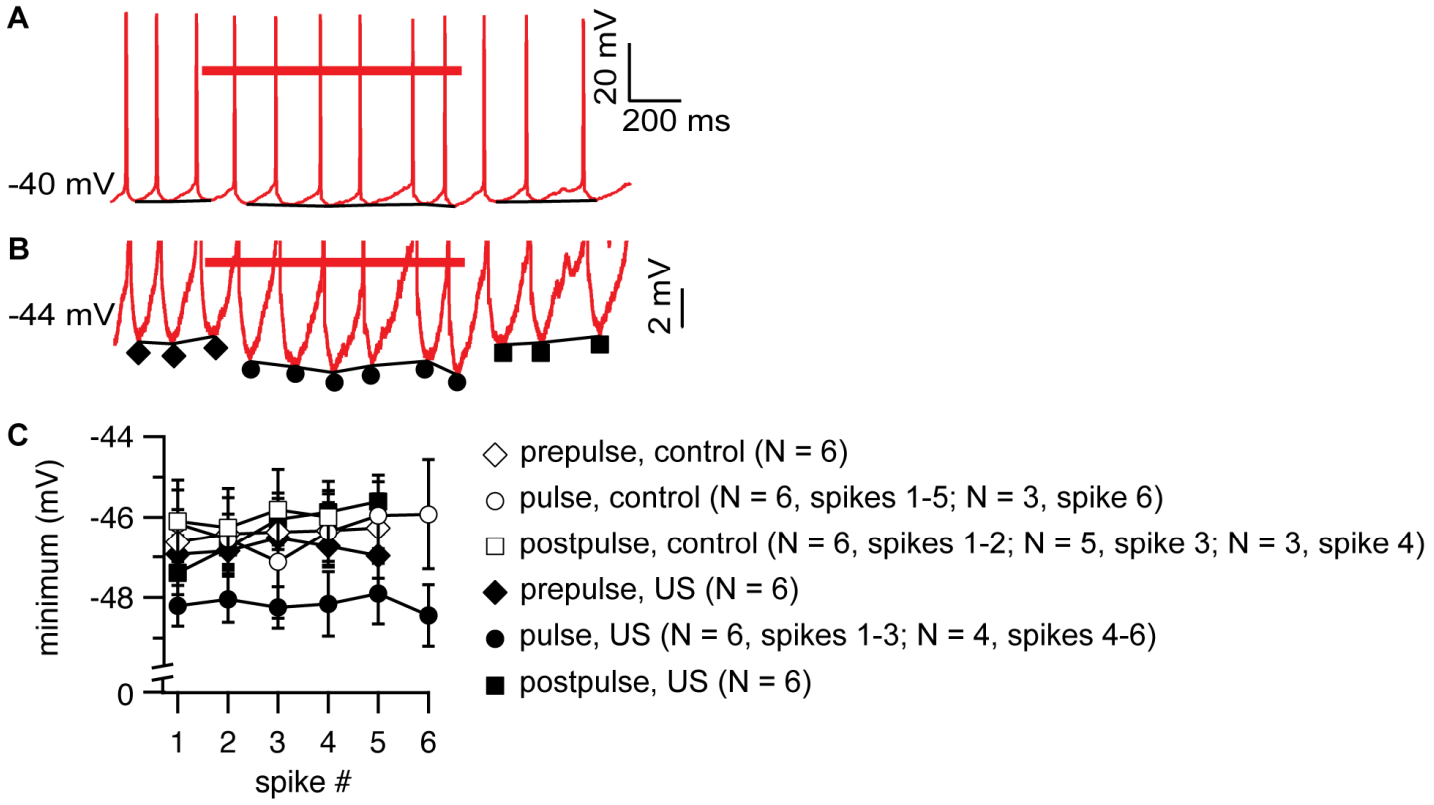

Figure 9. Ultrasound increases the depth of the afterhyperpolarization. A. Example voltage trace comparing voltage minima between action potentials in response to a 3-s, 250-pA current step with a 1-s ultrasound pulse (*red bar*) starting 1 s after the start of the current step. The *black lines* connect the voltage minima between action potentials before, during, or after the ultrasound pulse. **B.** Same as panel A, on a zoomed-in voltage scale. **C.** Mean (±SEM, N = 3-6 cells, see figure panel for details) values of the voltage minimum, as a function of action potential number, for the first four to six action potentials before (*solid diamonds*, 5 action potentials), during (*solid circles*, 6 action potentials), and after (*solid squares*, 5 action potentials) the ultrasound pulse, along with the equivalent mean values for the control condition (*open symbols*, 4, 6, and 5 action potentials). The means were determined for cells firing at the same average frequency (5 Hz) during a 1-s window starting 1 s after the start of the current step (corresponding to the period of the ultrasound stimulus) in the control condition. Significant differences between groups were only found in the presence of ultrasound ($P = 1.0 \times 10^{-4}$, 1.4×10^{-5}, and 0.16 for before versus during, during versus after, and before versus after the ultrasound pulse; P = 0.92, 0.39, and 0.35 for comparisons of the same time periods in the absence of ultrasound (unpaired, two-tailed Student's t-tests, unequal variance).

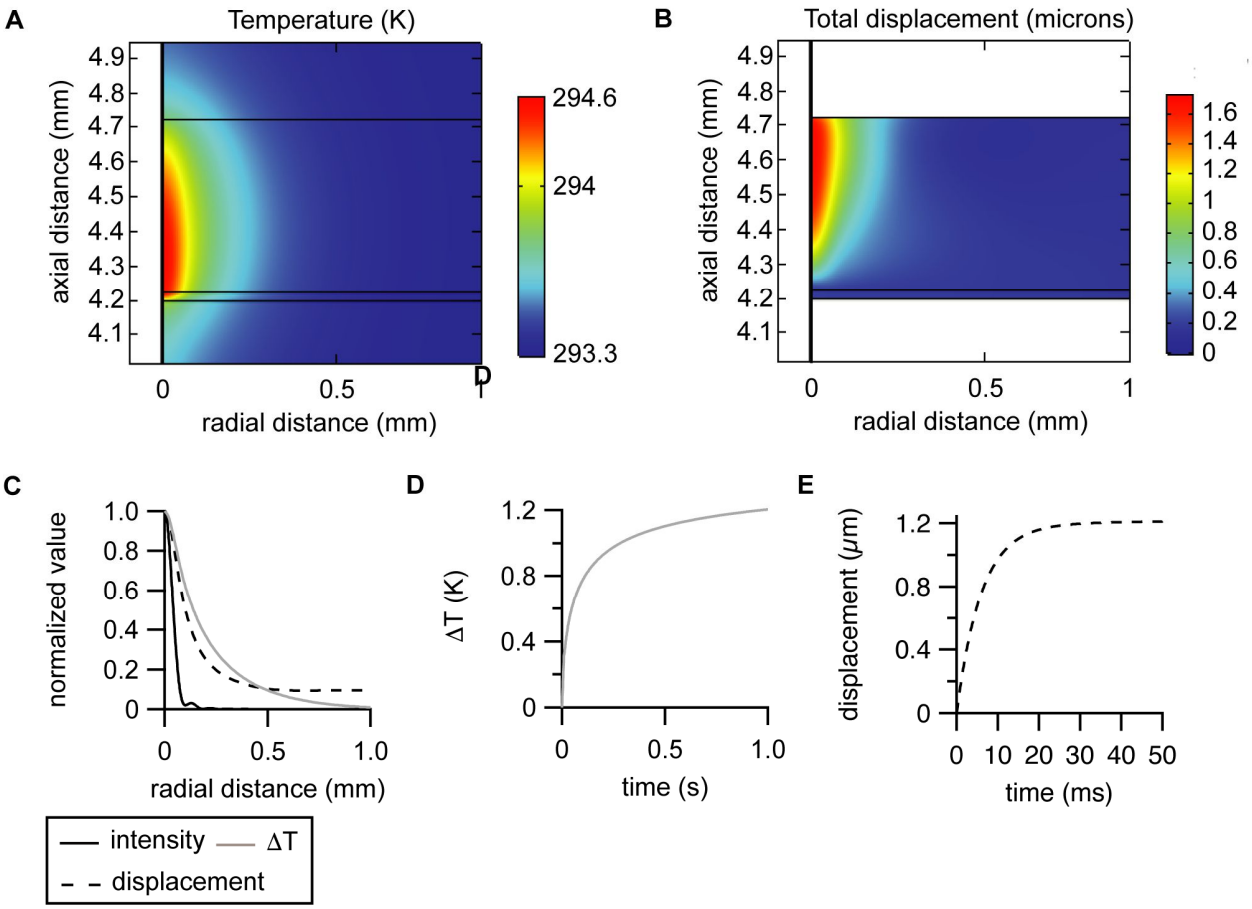

Figure 10. Simulated tissue heating and displacement in response to ultrasound. A. Spatial profile of temperature after one second of ultrasound exposure at 43 MHz and 50 W/cm^2, as a function of axial distance from the transducer surface and radial distance from the ultrasound beam axis, in a 500-micron thick brain slice and 25-micron thick polystyrene film (*middle two layers*) and the surrounding fluid (external solution, *top layer*, and distilled water, *bottom layer*). **B.** Spatial profile of the static total displacement in response to acoustic radiation force in the brain slice and polystyrene film. **C.** Normalized values of the acoustic intensity (*solid black line*), temperature rise after 1 second of ultrasound exposure (*solid gray line*), and total displacement (*dashed line*), at a depth of 250 microns in the brain slice, as a function of radial distance. **D.** Time course of the temperature rise in response at ultrasound at a depth of 250 microns in the brain slice on the axis of the ultrasound beam. The time course of the temperature change can be described by two exponential components with amplitudes and time constants of -0.56 C and 30 ms, and -0.57 C and 295 ms, for a weighted time constant of 164 ms. **E.** Time course of the displacement in response at ultrasound at a depth of 250 microns in the brain slice on the axis of the ultrasound beam. The time course of the displacement change can be described by two exponential components with amplitudes and time constants of -1.2 microns and 6 ms, and -0.13 microns and 344 ms, for a weighted time constant of 39 ms. Note that the steady-state displacement is slightly smaller than in the static displacement simulation due to the inclusion of the fluid loading in the dynamic displacement simulation.

REFERENCES

Abolfathi, N., A. Naik, M. Sotudeh Chafi, G. Karami, and M. Ziejewski. 2009. A micromechanical procedure for modelling the anisotropic mechanical properties of brain white matter. *Comput Methods Biomech Biomed Engin*. 12:249-262.

Alvarez, O., and R. Latorre. 1978. Voltage-dependent capacitance in lipid bilayers made from monolayers. *Biophys J*. 21:1-17.

Arbogast, K.B., and S.S. Margulies. 1999. A fiber-reinforced composite model of the viscoelastic behavior of the brainstem in shear. *J Biomech*. 32:865-870.

Bean, B.P. 2007. The action potential in mammalian central neurons. *Nat Rev Neurosci*. 8:451-465.

Beyder, A., J.L. Rae, C. Bernard, P.R. Strege, F. Sachs, and G. Farrugia. 2010. Mechanosensitivity of Nav1.5, a voltage-sensitive sodium channel. *J Physiol*. 588:4969-4985.

Blackmore, J., S. Shrivastava, J. Sallet, C.R. Butler, and R.O. Cleveland. 2019. Ultrasound Neuromodulation: A Review of Results, Mechanisms and Safety. *Ultrasound Med Biol*. 45:1509-1536.

Blanton, M.G., J.J. Lo Turco, and A.R. Kriegstein. 1989. Whole cell recording from neurons in slices of reptilian and mammalian cerebral cortex. *J Neurosci Methods*. 30:203-210.

Brickley, S.G., M.I. Aller, C. Sandu, E.L. Veale, F.G. Alder, H. Sambi, A. Mathie, and W. Wisden. 2007. TASK-3 two-pore domain potassium channels enable sustained high-frequency firing in cerebellar granule neurons. *J Neurosci*. 27:9329-9340.

Brohawn, S.G., Z. Su, and R. MacKinnon. 2014. Mechanosensitivity is mediated directly by the lipid membrane in TRAAK and TREK1 K+ channels. *Proc Natl Acad Sci U S A*. 111:3614-3619.

Brohawn, S.G., W. Wang, A. Handler, E.B. Campbell, J.R. Schwarz, and R. MacKinnon. 2019. The mechanosensitive ion channel TRAAK is localized to the mammalian node of Ranvier. *Elife*. 8.

Bystritsky, A., A.S. Korb, P.K. Douglas, M.S. Cohen, W.P. Melega, A.P. Mulgaonkar, A. DeSalles, B.K. Min, and S.S. Yoo. 2011. A review of low-intensity focused ultrasound pulsation. *Brain Stimul*. 4:125-136.

Calabrese, B., I.V. Tabarean, P. Juranka, and C.E. Morris. 2002. Mechanosensitivity of N-type calcium channel currents. *Biophys J*. 83:2560-2574.

Calhoun, M.A., S.A. Bentil, E. Elliott, J.J. Otero, J.O. Winter, and R.B. Dupaix. 2019. Beyond linear elastic modulus: viscoelastic models for brain and brain mimetic hydrogels. *ACS Biomaterials Science & Engineering*. 5:3964-3973.

Castaneda-Castellanos, D.R., A.C. Flint, and A.R. Kriegstein. 2006. Blind patch clamp recordings in embryonic and adult mammalian brain slices. *Nat Protoc*. 1:532-542.

Colucci, V., G. Strichartz, F. Jolesz, N. Vykhodtseva, and K. Hynynen. 2009. Focused ultrasound effects on nerve action potential in vitro. *Ultrasound Med Biol*. 35:1737-1747.

Company, C.R. 1965. Handbook of Chemistry and Physics. 45th.ed. Chemical Rubber Compnay, Cleveland, OH.

Cotero, V., Y. Fan, T. Tsaava, A.M. Kressel, I. Hancu, P. Fitzgerald, K. Wallace, S. Kaanumalle, J. Graf, W. Rigby, T.J. Kao, J. Roberts, C. Bhushan, S. Joel, T.R. Coleman, S. Zanos, K.J. Tracey, J. Ashe, S.S. Chavan, and C. Puleo. 2019. Noninvasive sub-organ ultrasound stimulation for targeted neuromodulation. *Nat Commun*. 10:952.

Darrow, D.P., P. O'Brien, T.J. Richner, T.I. Netoff, and E.S. Ebbini. 2019. Reversible neuroinhibition by focused ultrasound is mediated by a thermal mechanism. *Brain Stimul*. 12:1439-1447.

de Korte, C.L., A.F. van der Steen, and J.M. Thijssen. 1994. Acoustic velocity and attenuation of eye tissues at 20 MHz. *Ultrasound Med Biol*. 20:471-480.

Downs, M.E., S.A. Lee, G. Yang, S. Kim, Q. Wang, and E.E. Konofagou. 2018. Non-invasive peripheral nerve stimulation via focused ultrasound in vivo. *Phys Med Biol*. 63:035011.

Duck, F.A. 1998. Radiation pressure and acoustic streaming. *In* Ultrasound in Medicine. F. Duck, A. Baker and H. Starritt, editors. Institute of Physics Publishing, Philadelphia, PA.

Duke, A.R., M.W. Jenkins, H. Lu, J.M. McManus, H.J. Chiel, and E.D. Jansen. 2013. Transient and selective suppression of neural activity with infrared light. *Sci Rep*. 3:2600.

Evans, E.A., R. Waugh, and L. Melnik. 1976. Elastic area compressibility modulus of red cell membrane. *Biophys J*. 16:585-595.

Fomenko, A., C. Neudorfer, R.F. Dallapiazza, S.K. Kalia, and A.M. Lozano. 2018. Low-intensity ultrasound neuromodulation: An overview of mechanisms and emerging human applications. *Brain Stimul*. 11:1209-1217.

Fry, F.J., H.W. Ades, and W.J. Fry. 1958. Production of reversible changes in the central nervous system by ultrasound. *Science*. 127:83-84.
Gaur, U., and B. Wunderlich. 1982. Heat-Capacity and Other Thermodynamic Properties of Linear Macromolecules .5. Polystyrene. *J Phys Chem Ref Data*. 11:313-325.
Gavrilov, L.R., E.M. Tsirulnikov, and I.A. Davies. 1996. Application of focused ultrasound for the stimulation of neural structures. *Ultrasound Med Biol*. 22:179-192.
Giese, K.P., J.F. Storm, D. Reuter, N.B. Fedorov, L.R. Shao, T. Leicher, O. Pongs, and A.J. Silva. 1998. Reduced K+ channel inactivation, spike broadening, and after-hyperpolarization in Kvbeta1.1-deficient mice with impaired learning. *Learn Mem*. 5:257-273.
Gu, N., K. Vervaeke, and J.F. Storm. 2007. BK potassium channels facilitate high-frequency firing and cause early spike frequency adaptation in rat CA1 hippocampal pyramidal cells. *J Physiol*. 580:859-882.
Hand, J.W. 1998. Ultrasound hyperthermia and the prediction of heating. *In* Ultrasound in Medicine. F. Duck, A. Baker and H. Starritt, editors. Institute of Physics Publishing, Philadelphia, PA.
Harper, C.A. 2006. Handbook of plastics technologies: the complete guide to properties and performance. *In*. McGraw-Hill, New York, NY.
Hille, B. 2001. Ion Channels of Excitable Membranes. 3rd
.ed. Sinauer Associates, Inc., Sunderland, MA.
Kanda, H., J. Ling, S. Tonomura, K. Noguchi, S. Matalon, and J.G. Gu. 2019. TREK-1 and TRAAK Are Principal K(+) Channels at the Nodes of Ranvier for Rapid Action Potential Conduction on Mammalian Myelinated Afferent Nerves. *Neuron*. 104:960-971 e967.
Kang, D., C. Choe, and D. Kim. 2005. Thermosensitivity of the two-pore domain K+ channels TREK-2 and TRAAK. *J Physiol*. 564:103-116.
Khaliq, Z.M., and B.P. Bean. 2010. Pacemaking in dopaminergic ventral tegmental area neurons: depolarizing drive from background and voltage-dependent sodium conductances. *J Neurosci*. 30:7401-7413.
Kim, J., D.S. Wei, and D.A. Hoffman. 2005. Kv4 potassium channel subunits control action potential repolarization and frequency-dependent broadening in rat hippocampal CA1 pyramidal neurones. *J Physiol*. 569:41-57.
King, R.L., J.R. Brown, W.T. Newsome, and K.B. Pauly. 2013. Effective parameters for ultrasound-induced in vivo neurostimulation. *Ultrasound Med Biol*. 39:312-331.
Kole, M.H. 2011. First node of Ranvier facilitates high-frequency burst encoding. *Neuron*. 71:671-682.
Krasovitski, B., V. Frenkel, S. Shoham, and E. Kimmel. 2011. Intramembrane cavitation as a unifying mechanism for ultrasound-induced bioeffects. *Proc Natl Acad Sci U S A*. 108:3258-3263.
Kubanek, J., J. Shi, J. Marsh, D. Chen, C. Deng, and J. Cui. 2016. Ultrasound modulates ion channel currents. *Sci Rep*. 6:24170.
Kwok, R., and E. Evans. 1981. Thermoelasticity of large lecithin bilayer vesicles. *Biophys J*. 35:637-652.
Laitko, U., and C.E. Morris. 2004. Membrane tension accelerates rate-limiting voltage-dependent activation and slow inactivation steps in a Shaker channel. *J Gen Physiol*. 123:135-154.
Lee, S.A., H.A.S. Kamimura, M.T. Burgess, and E.E. Konofagou. 2020. Displacement imaging for focused ultrasound peripheral nerve neuromodulation. *IEEE Trans Med Imaging*.
Leighton, T.G. 1998. An introduction to acoustic cavitation. *In* Ultrasound in Medicine. F. Duck, A. Baker and H. Starritt, editors. Institute of Physics Publishing, Philadelphia, PA.
Leterrier, C. 2018. The Axon Initial Segment: An Updated Viewpoint. *J Neurosci*. 38:2135-2145.
Lien, C.C., and P. Jonas. 2003. Kv3 potassium conductance is necessary and kinetically optimized for high-frequency action potential generation in hippocampal interneurons. *J Neurosci*. 23:2058-2068.
Liu, P.W., and B.P. Bean. 2014. Kv2 channel regulation of action potential repolarization and firing patterns in superior cervical ganglion neurons and hippocampal CA1 pyramidal neurons. *J Neurosci*. 34:4991-5002.
Lothet, E.H., K.M. Shaw, H. Lu, J. Zhuo, Y.T. Wang, S. Gu, D.B. Stolz, E.D. Jansen, C.C. Horn, H.J. Chiel, and M.W. Jenkins. 2017. Selective inhibition of small-diameter axons using infrared light. *Sci Rep*. 7:3275.
Madison, D.V., and R.A. Nicoll. 1984. Control of the repetitive discharge of rat CA 1 pyramidal neurones in vitro. *J Physiol*. 354:319-331.
Maingret, F., I. Lauritzen, A.J. Patel, C. Heurteaux, R. Reyes, F. Lesage, M. Lazdunski, and E. Honore. 2000. TREK-1 is a heat-activated background K(+) channel. *EMBO J*. 19:2483-2491.
Malinow, R., and R.W. Tsien. 1990. Presynaptic enhancement shown by whole-cell recordings of long-term potentiation in hippocampal slices. *Nature*. 346:177-180.

Marinc, C., C. Derst, H. Pruss, and R.W. Veh. 2014. Immunocytochemical localization of TASK-3 protein (K2P9.1) in the rat brain. *Cell Mol Neurobiol*. 34:61-70.

Menz, M.D., O. Oralkan, P.T. Khuri-Yakub, and S.A. Baccus. 2013. Precise neural stimulation in the retina using focused ultrasound. *J Neurosci*. 33:4550-4560.

Menz, M.D., P. Ye, K. Firouzi, A. Nikoozadeh, K.B. Pauly, P. Khuri-Yakub, and S.A. Baccus. 2019. Radiation Force as a Physical Mechanism for Ultrasonic Neurostimulation of the Ex Vivo Retina. *J Neurosci*. 39:6251-6264.

Mihran, R.T., F.S. Barnes, and H. Wachtel. 1990. Temporally-specific modification of myelinated axon excitability in vitro following a single ultrasound pulse. *Ultrasound Med Biol*. 16:297-309.

Min, B.K., A. Bystritsky, K.I. Jung, K. Fischer, Y. Zhang, L.S. Maeng, S.I. Park, Y.A. Chung, F.A. Jolesz, and S.S. Yoo. 2011. Focused ultrasound-mediated suppression of chemically-induced acute epileptic EEG activity. *BMC Neurosci*. 12:23.

Morris, C.E., and P.F. Juranka. 2007. Nav channel mechanosensitivity: activation and inactivation accelerate reversibly with stretch. *Biophys J*. 93:822-833.

Needham, D., and R.S. Nunn. 1990. Elastic deformation and failure of lipid bilayer membranes containing cholesterol. *Biophys J*. 58:997-1009.

Owen, S.F., M.H. Liu, and A.C. Kreitzer. 2019. Thermal constraints on in vivo optogenetic manipulations. *Nat Neurosci*. 22:1061-1065.

Pan, Z., T. Kao, Z. Horvath, J. Lemos, J.Y. Sul, S.D. Cranstoun, V. Bennett, S.S. Scherer, and E.C. Cooper. 2006. A common ankyrin-G-based mechanism retains KCNQ and NaV channels at electrically active domains of the axon. *J Neurosci*. 26:2599-2613.

Paris, L., I. Marc, B. Charlot, M. Dumas, J. Valmier, and F. Bardin. 2017. Millisecond infrared laser pulses depolarize and elicit action potentials on in-vitro dorsal root ganglion neurons. *Biomed Opt Express*. 8:4568-4578.

Plaksin, M., E. Kimmel, and S. Shoham. 2016. Cell-Type-Selective Effects of Intramembrane Cavitation as a Unifying Theoretical Framework for Ultrasonic Neuromodulation. *eNeuro*. 3.

Prieto, M.L., K. Firouzi, B.T. Khuri-Yakub, and M. Maduke. 2018. Activation of Piezo1 but Not NaV1.2 Channels by Ultrasound at 43 MHz. *Ultrasound Med Biol*. 44:1217-1232.

Prieto, M.L., O. Oralkan, B.T. Khuri-Yakub, and M.C. Maduke. 2013. Dynamic response of model lipid membranes to ultrasonic radiation force. *PLoS One*. 8:e77115.

Rashid, B., M. Destrade, and M.D. Gilchrist. 2012. Mechanical characterization of brain tissue in compression at dynamic strain rates. *J Mech Behav Biomed Mater*. 10:23-38.

Rashid, B., M. Destrade, and M.D. Gilchrist. 2013. Mechanical characterization of brain tissue in simple shear at dynamic strain rates. *J Mech Behav Biomed Mater*. 28:71-85.

Ricca, B.L., G. Venugopalan, and D.A. Fletcher. 2013. To pull or be pulled: parsing the multiple modes of mechanotransduction. *Curr Opin Cell Biol*. 25:558-564.

Richter, C.P., A.I. Matic, J.D. Wells, E.D. Jansen, and J.T. Walsh, Jr. 2011. Neural stimulation with optical radiation. *Laser Photon Rev*. 5:68-80.

Sarvazyan, A.P., O.V. Rudenko, and W.L. Nyborg. 2010. Biomedical applications of radiation force of ultrasound: historical roots and physical basis. *Ultrasound Med Biol*. 36:1379-1394.

Seeger, H.M., L. Aldrovandi, A. Alessandrini, and P. Facci. 2010. Changes in single K(+) channel behavior induced by a lipid phase transition. *Biophys J*. 99:3675-3683.

Selfridge, A.R. 1985. Approximate Material Properties in Isotropic Materials. *Ieee T Son Ultrason*. 32:381-394.

Shah, M.M., M. Migliore, I. Valencia, E.C. Cooper, and D.A. Brown. 2008. Functional significance of axonal Kv7 channels in hippocampal pyramidal neurons. *Proc Natl Acad Sci U S A*. 105:7869-7874.

Shao, L.R., R. Halvorsrud, L. Borg-Graham, and J.F. Storm. 1999. The role of BK-type Ca2+-dependent K+ channels in spike broadening during repetitive firing in rat hippocampal pyramidal cells. *J Physiol*. 521 Pt 1:135-146.

Shapiro, M.G., K. Homma, S. Villarreal, C.P. Richter, and F. Bezanilla. 2012. Infrared light excites cells by changing their electrical capacitance. *Nat Commun*. 3:736.

Tabarean, I.V., and C.E. Morris. 2002. Membrane stretch accelerates activation and slow inactivation in Shaker channels with S3-S4 linker deletions. *Biophys J*. 82:2982-2994.

Talley, E.M., G. Solorzano, Q. Lei, D. Kim, and D.A. Bayliss. 2001. Cns distribution of members of the two-pore-domain (KCNK) potassium channel family. *J Neurosci*. 21:7491-7505.

Taverna, S., T. Tkatch, A.E. Metz, and M. Martina. 2005. Differential expression of TASK channels between horizontal interneurons and pyramidal cells of rat hippocampus. *J Neurosci*. 25:9162-9170.
Taylor, R.E. 1965. Impedance of the squid axon membrane. *J Cell Comp Physiol*. 66:21-25.
Thijssen, J.M., H.J. Mol, and M.R. Timmer. 1985. Acoustic parameters of ocular tissues. *Ultrasound Med Biol*. 11:157-161.
Tsui, P.H., S.H. Wang, and C.C. Huang. 2005. In vitro effects of ultrasound with different energies on the conduction properties of neural tissue. *Ultrasonics*. 43:560-565.
Tufail, Y., A. Matyushov, N. Baldwin, M.L. Tauchmann, J. Georges, A. Yoshihiro, S.I. Tillery, and W.J. Tyler. 2010. Transcranial pulsed ultrasound stimulates intact brain circuits. *Neuron*. 66:681-694.
Tyler, W.J., Y. Tufail, M. Finsterwald, M.L. Tauchmann, E.J. Olson, and C. Majestic. 2008. Remote excitation of neuronal circuits using low-intensity, low-frequency ultrasound. *PLoS One*. 3:e3511.
Walsh, A.J., G.P. Tolstykh, S. Martens, B.L. Ibey, and H.T. Beier. 2016. Action potential block in neurons by infrared light. *Neurophotonics*. 3:040501.
Wang, J., and O.P. Hamill. 2020. Piezo2, a pressure sensitive channel is expressed in select neurons of the mouse brain: a putative mechanism for synchronizing neural networks by transducing intracranial pressure pulses. *bioRxiv*.
Wells, J., C. Kao, P. Konrad, T. Milner, J. Kim, A. Mahadevan-Jansen, and E.D. Jansen. 2007. Biophysical mechanisms of transient optical stimulation of peripheral nerve. *Biophys J*. 93:2567-2580.
White, S.H., and T.E. Thompson. 1973. Capacitance, area, and thickness variations in thin lipid films. *Biochim Biophys Acta*. 323:7-22.
Wu, J., and W.L. Nyborg. 2008. Ultrasound, cavitation bubbles and their interaction with cells. *Adv Drug Deliv Rev*. 60:1103-1116.
Yamada-Hanff, J., and B.P. Bean. 2015. Activation of Ih and TTX-sensitive sodium current at subthreshold voltages during CA1 pyramidal neuron firing. *J Neurophysiol*. 114:2376-2389.
Ye, P.P., J.R. Brown, and K.B. Pauly. 2016. Frequency Dependence of Ultrasound Neurostimulation in the Mouse Brain. *Ultrasound Med Biol*. 42:1512-1530.
Young, R.R., and E. Henneman. 1961. Functional effects of focused ultrasound on mammalian nerves. *Science*. 134:1521-1522.
Yue, C., and Y. Yaari. 2004. KCNQ/M channels control spike afterdepolarization and burst generation in hippocampal neurons. *J Neurosci*. 24:4614-4624.
Zachs, D.P., S.J. Offutt, R.S. Graham, Y. Kim, J. Mueller, J.L. Auger, N.J. Schuldt, C.R.W. Kaiser, A.P. Heiller, R. Dutta, H. Guo, J.K. Alford, B.A. Binstadt, and H.H. Lim. 2019. Noninvasive ultrasound stimulation of the spleen to treat inflammatory arthritis. *Nat Commun*. 10:951.
Zhou, D., S. Lambert, P.L. Malen, S. Carpenter, L.M. Boland, and V. Bennett. 1998. AnkyrinG is required for clustering of voltage-gated Na channels at axon initial segments and for normal action potential firing. *J Cell Biol*. 143:1295-1304.
Zhu, X., J.W. Lin, and M.Y. Sander. 2019. Infrared inhibition and waveform modulation of action potentials in the crayfish motor axon. *Biomed Opt Express*. 10:6580-6594.

SUPPLEMENTAL MATERIALS

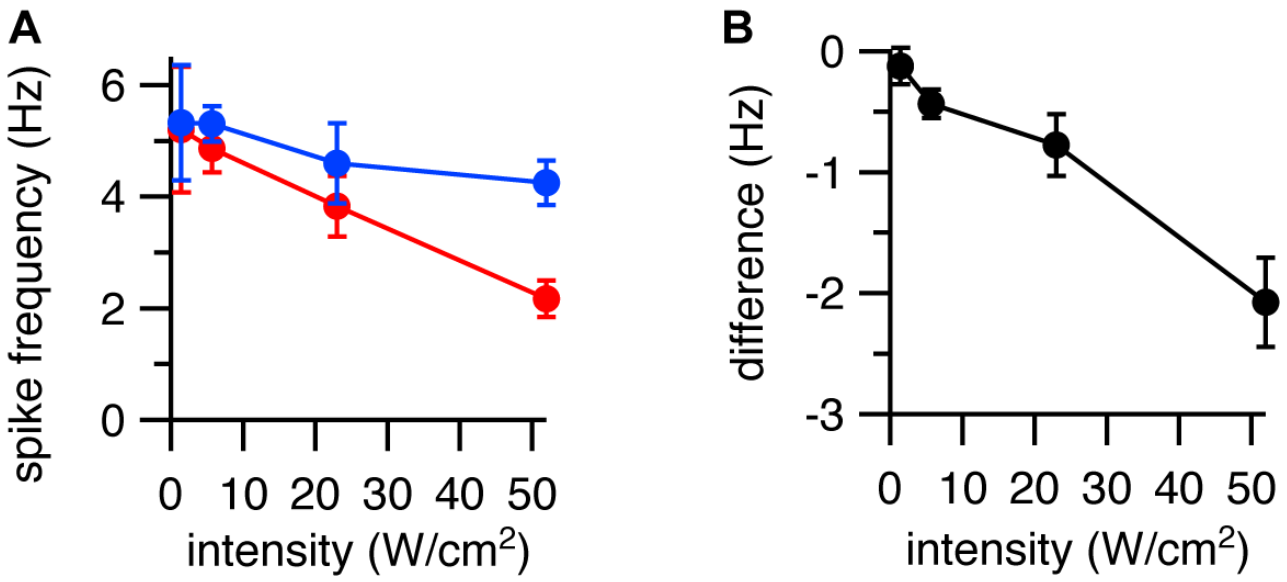

Supplemental Figure 1. Effects of ultrasound at different intensities on firing rate. A. Mean (± SEM) action potential firing rate with (*red*) or without (*blue*) a 1-s ultrasound pulse at various intensities starting 200 ms after the start of a 2-s current step, as measured during the period of overlap between the ultrasound and current stimuli, or during the same time period in the absence of ultrasound. N = 4 cells, except for 6 W/cm^2, where N = 3 cells. **B.** As in panel A, but showing the difference in firing rate between the ultrasound and control conditions.

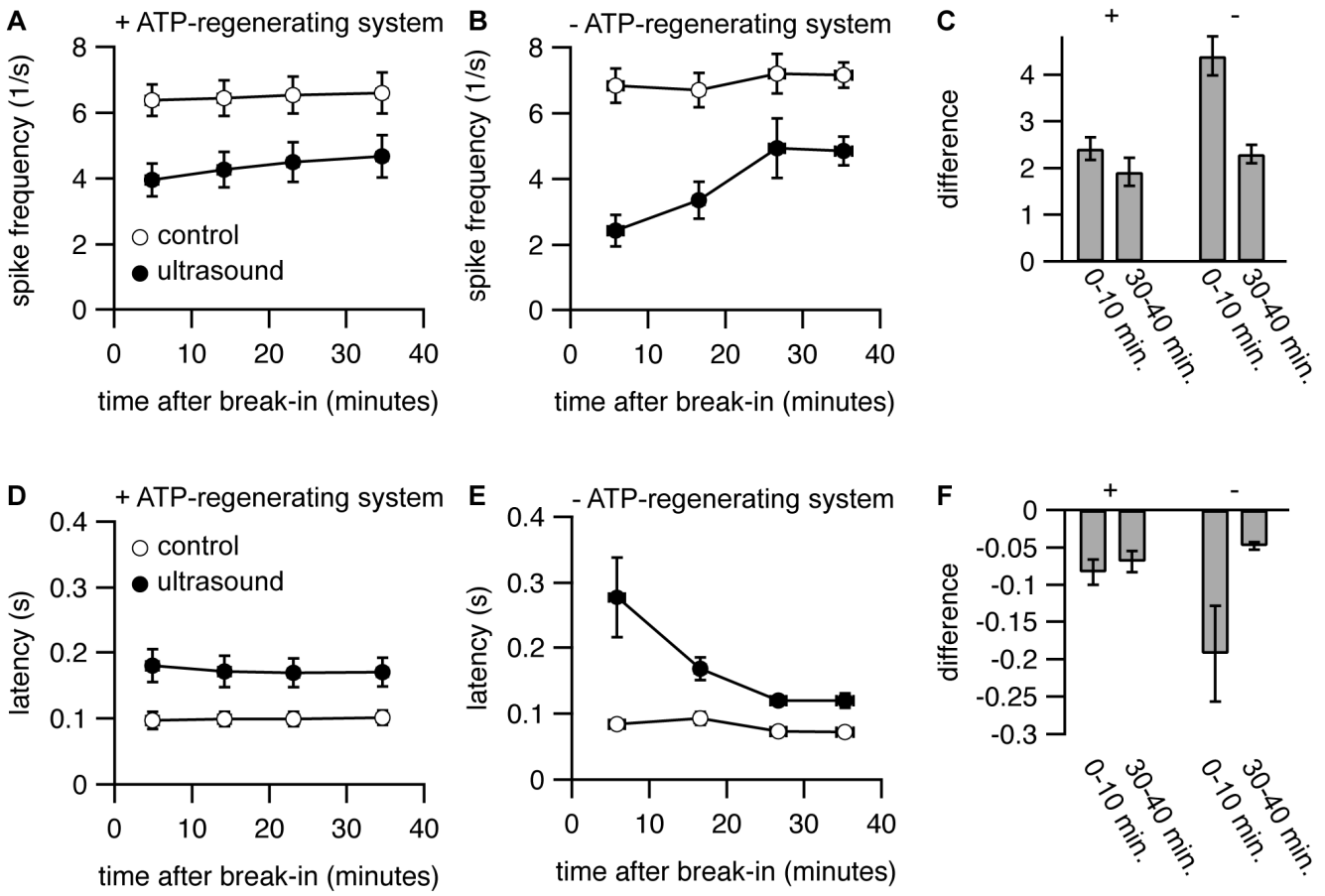

Supplemental Figure 2. An ATP-regenerating internal solution stabilizes the response to ultrasound. A-B. Mean (±SEM) spike rates during the first 500 ms of a current step in the presence (*solid circles*) and absence (*open circles*) of a 1-s ultrasound application starting 500 ms before the current step, as a function of time relative to break-in (establishment of whole-cell recording configuration). The internal solution contained 10 Na-phosphocreatine with (A) or without (B) 50 U/mL creatine phosphokinase to provide an ATP-regenerating system. Spike rates were measured at various time points between 0 and 10, 10 and 20, 20 and 30, and 30 and 40 minutes after break-in. The x-values represent the mean start time for the protocol to measure spike rates (which comprised 2 minutes of recording time) with horizontal error bars (in some cases smaller than the symbol size) representing the SEM. The amplitude of the current step was adjusted over time to maintain spiking behavior as close as possible to that at the start of the experiment. **C.** Mean (±SEM) difference in spike rate between the control and ultrasound conditions for measurements at 1-10 minutes after break-in and 30-40 minutes after break-in, with (*left*) or without (*right*) the ATP-regenerating system. The difference was only statistically significant without the ATP-regenerating system (P = 0.11, with; and P = 0.0064, without). **D-F.** Same as A-B, but for latency to the first action potential following the start of the current step. N = 10 cells with and N = 6 cells without the ATP-regenerating system. The difference was not statistically significant for either group (P = 0.21, with; and P = 0.089, without).

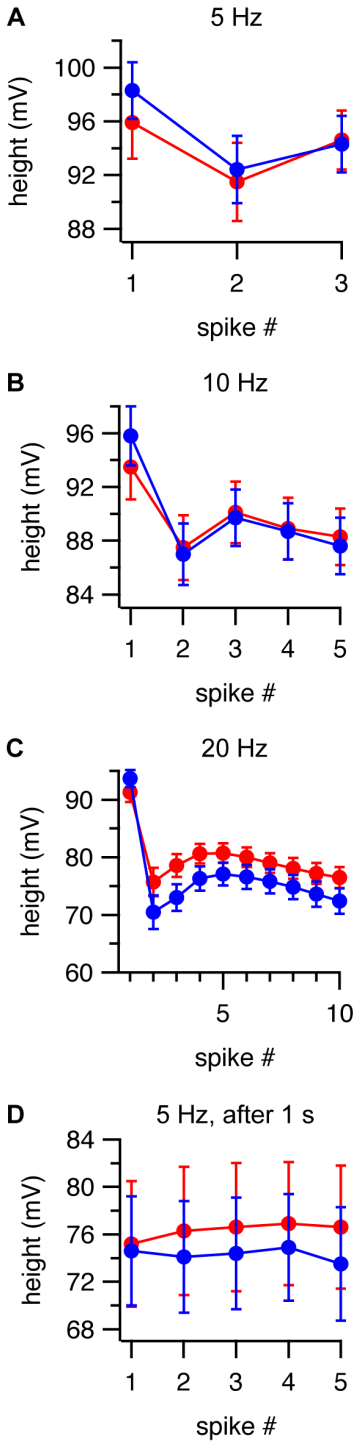

Supplemental Figure 3. Effects of ultrasound on action potential height. A-C. Mean (±SEM) action potential heights as a function of action potential number in the presence (*red*) and absence (*blue*) of a 1-s ultrasound pulse starting 500 ms before the current step, for cells firing at an average firing rates (as measured during the first 500 ms of the current step) of approximately 5 Hz (N = 13), 10 Hz (N = 15), and 20 Hz (N = 13) in the control condition. **D.** As in A-C, but with ultrasound applied 1 s after the start of a 3-s current step, for cells firing at an average firing rate of approximately 5 Hz in the control condition, with firing rate determined in a 1-s window starting 1 s after the current step (corresponding to the time period of the ultrasound stimulus), and action potential number relative to the start of the ultrasound stimulus (N = 6). Note that the y-axes do not begin at zero.